

# Wind Effects Induced by Multivortex Tornadoes on a Low-Rise Building

Yi Zhao, Ph.D.<sup>1</sup>; Guirong Yan, Ph.D., F.ASCE<sup>2</sup>;  
Tetsuya Takemi, Ph.D.<sup>3</sup>; and John van de Lindt, Ph.D., F.ASCE<sup>4</sup>

**Abstract:** Multivortex tornadoes contain two or more subvortices that orbit within a parent vortex and can generate highly intermittent and localized near-ground wind fields. This study investigates how tornado flow structure affects wind effects on a low-rise building using large-eddy simulations. One single-vortex tornado and three multivortex tornadoes with different subvortex configurations are examined by systematically varying swirl ratio. Tornado translation is modeled using a relative-motion framework in which the building traverses the vortex field. Aerodynamic force and moment coefficients are evaluated along the traversing path. Additional stationary simulations are conducted to examine repeated load amplification associated with subvortex passages. Compared with the single-vortex case, multivortex tornadoes produce substantially larger uplift and more complex temporal responses, characterized by multiple peak groups linked to sequential interactions with orbiting subvortices. Surface pressure analysis indicates a transition from wind-speed-driven suction to dominance of localized pressure deficits within subvortex cores. The results suggest the need to explicitly account for multivortex tornado dynamics when characterizing tornado-induced wind effects. DOI: [10.1061/JSENDH.STENG-15912](https://doi.org/10.1061/JSENDH.STENG-15912). © 2026 American Society of Civil Engineers.

## Introduction

The United States experiences approximately 1,200 tornadoes annually, resulting in significant casualties and property damage that often exceeds hurricane-related losses. In fact, extreme wind events such as tornadoes generate significantly different loading conditions compared to conventional straight-line winds due to their distinct flow characteristics, particularly their strong tangential velocity and vertical velocity components. While experimental testing in low-speed boundary-layer wind tunnels remains valuable for understanding wind loads, recent research has expanded our understanding of tornado–structure interactions. Studies utilizing Ward-type tornado simulators with small-scale building models have demonstrated that tornado-like vortices generate higher surface pressures than equivalent straight-line winds (Chang 1971; Jischke and Light 1983; Bienkiewicz and Duhia 1993; Fouts et al. 2003; Mishra et al. 2008). Further investigations incorporating vortex translation have revealed its significant influence on structural wind loads (Sengupta et al. 2008; Haan et al. 2010).

However, these studies have primarily focused on single-vortex tornadoes, either single-celled or double-celled, while neglecting the complex dynamics of multivortex tornadoes. Multivortex

tornadoes, which contain two or more subvortices rotating around a common center, have been observed for over five decades. Fujita (1970) first identified “suction spots”—highly localized regions of intense damage—based on aerial damage surveys, which he later reclassified as “suction vortices” (Fujita 1981). Since then, numerous studies have confirmed the presence of multivortex structures in both observational and experimental settings (Agee et al. 1976; Ipauley and Snow 1988). The Spencer, South Dakota, tornado of 1998 provided the first direct radar evidence of such vortices (Wurman 1999), and subsequent Doppler radar studies have continued to reveal their complexity and prevalence (Wurman 2002; Bluestein et al. 2015).

Importantly, tornadoes are not static in flow structure; a single tornado may alternate between single-vortex and multivortex phases during its lifecycle. Bluestein et al. (2018) observed that these secondary vortices—typically 1–10 m in scale—can form within the broader 100 m–1 km-scale parent vortex and rotate cyclonically around the center. These transitions are influenced by local swirl ratios and instability in the shear layers near the radius of maximum wind (Church et al. 1979; Rotunno 2013). Laboratory studies have shown that increasing swirl ratio promotes the formation of these secondary vortices (Davies-Jones et al. 2001; Lewellen et al. 2000). Several destructive tornadoes have been identified as multivortex events. The 2011 Joplin, Missouri, tornado included multiple subvortices, resulting in 161 fatalities and \$2.8 billion in losses (Kuligowski et al. 2014). The 2013 El Reno, Oklahoma, tornado, the widest tornado on record, contained multiple condensation funnels and rapid vortex transitions documented by multiple radar platforms (Bluestein et al. 2015; Wakimoto et al. 2016). During this tornado, even experienced storm chasers were overtaken by unanticipated subvortices, highlighting the danger posed by this multivortex flow structure (Wurman et al. 2014). In summary, multivortex tornadoes are very common. However, the current research on tornadic wind effects or wind loading determination all assume that the tornado has a single vortex. This motivated the present authors to bridge this research gap, by studying the wind effects on a low-rise building induced by multivortex tornadoes and comparing it with those induced by single-vortex tornadoes. If the wind effects induced

<sup>1</sup>Postdoctoral Researcher, Dept. of Civil, Architectural and Environmental Engineering, Missouri Univ. of Science and Technology, Rolla, Missouri 65409. Email: yzvxs@mst.edu

<sup>2</sup>Professor, Dept. of Civil, Architectural and Environmental Engineering, Missouri Univ. of Science and Technology, Rolla, Missouri 65409 (corresponding author). Email: yang@mst.edu

<sup>3</sup>Professor, Disaster Prevention Research Institute, Kyoto Univ., Kyoto 611-0011, Japan. ORCID: <https://orcid.org/0000-0002-7596-2373>. Email: takemi@storm.dpri.kyoto-u.ac.jp

<sup>4</sup>Harold H. Short Endowed Chair Professor, Dept. of Civil and Environmental Engineering, Colorado State Univ., Fort Collins, CO 80523-1372. Email: John.van\_de\_Lindt@colostate.edu

Note. This manuscript was submitted on August 28, 2025; approved on March 2, 2026; published online on **No EPub Date XXXX XX**. Discussion period open until **No Discussion Date XX**; separate discussions must be submitted for individual papers. This paper is part of the *Journal of Structural Engineering*, © ASCE, ISSN 0733-9445.

74 by a multivortex tornado are much higher than a single-vortex tor- 136  
75 nado, the assumption of the single-vortex flow structure in the code 137  
76 development of the tornado-resistant design may not be proper. 138

77 Numerical modeling studies, particularly those simulating 139  
78 laboratory-scale tornado-like vortices, have extended these insights. 140  
79 Liu and Ishihara (2015) conducted large-eddy simulations (LESs) 141  
80 of translating tornado-like vortices and demonstrated how varying 142  
81 swirl ratios influenced the formation and motion of multiple sub- 4  
82 vortices. Gairola and Bitsuamlak (2019) developed a simplified 143  
83 computational fluid dynamics (CFD)-based tornado model that 144  
84 reproduced laboratory-scale tornado-like vortices and demonstra- 145  
85 ted how flow characteristics depend more directly on velocity field 146  
86 parameters than on simulator geometry. Zhao et al. (2021, 2023) 147  
87 expanded on this work by systematically investigating the role of 148  
88 swirl ratio and radial Reynolds number in producing multivortex 149  
89 regimes and dynamic flow interactions near the ground. Zhang 150  
90 et al. (2023) further examined the combined influence of swirl ratio 151  
91 and aspect ratio, showing how both geometric and flow conditions 152  
92 shape the formation, intensity, and near-surface behavior of multiple 153  
93 subvortices. However, most of previous studies on multivortex 154  
94 tornadoes focused on tornado vortex structure and localized wind 155  
95 field behavior; the research on tornadic wind effects on low-rise 156  
96 buildings induced by translating multivortex tornadoes is lacking. 157  
97 In related efforts, Yuan et al. (2019) applied LES to simulate 158  
98 a laboratory tornado simulator capable of producing translating 159  
99 tornado-like flow, offering insights into the combined effects of 160  
100 swirl ratio, translation, and ground interaction. Honerkamp et al. 161  
101 (2022) numerically modeled tornado-induced flow around bluff 162  
102 bodies and showed how changes in tornadic wind flow structure 163  
103 affect pressure distributions on building surfaces. 164

104 In addition, although prior studies have characterized tornado- 165  
105 induced wind loads (Case et al. 2014; Cao et al. 2018; Razavi and 166  
106 Sarkar 2021; Honerkamp et al. 2022; Li et al. 2023; Dang et al. 167  
107 2023; Zhao et al. 2023), most of them have focused on a single 168  
108 type of tornado flow structure, mainly a single-vortex configuration. 169  
109 There remains limited understanding of how different tornado 170  
110 flow structures, such as single-vortex versus multivortex tornadoes 171  
111 with varying numbers of subvortices, different swirl ratios, and 172  
112 different core sizes, affect the tornado-induced wind loading on 173  
113 structures. These differences are particularly important given the 174  
114 spatial and temporal variability introduced by multiple interacting 175  
115 vortices, which can result in highly localized peak pressures and 176  
116 asymmetric force distributions. The present study addresses this gap 177  
117 by systematically studying and comparing wind-induced pressure 178  
118 and force distributions on a low-rise building subjected to four 179  
119 tornadoes with distinct flow structures—one single-vortex and three 180  
120 multivortex cases with varying subvortex configurations. This study 181  
121 will provide new insights into shortcomings in current design 182  
122 provisions that assume a single-vortex flow structure. 183

123 The primary objectives of this study are to: (1) characterize the 184  
124 near-ground wind flow features and surface pressure distributions 185  
125 associated with multivortex tornadoes using high-fidelity CFD sim- 186  
126 ulations; (2) elucidate the differences in wind-effect mechanisms 187  
127 acting on a low-rise building between single-vortex and multivortex 188  
128 tornadoes, with particular emphasis on the role of orbiting subvorti- 189  
129 ces in producing transient load amplification and spatially localized 190  
130 pressures; and (3) provide mechanistic insight into how tornado 191  
131 flow structure governs the magnitude, temporal variability, and 192  
132 governing modes of wind effects on low-rise buildings. 193

## 133 CFD Simulation Setup and Validation

134 In this study, the computational software ANSYS FLUENT 2021 194  
135 is used. In the authors' previous work, the Spencer, SD, tornado of 195

136 30 May 1998, for the stage with the flow structure of double-celled 137  
138 single-vortex, has been successfully simulated and validated by 139  
140 using the radar-measured velocity data. Based on this model, the 141  
142 boundary conditions of the computational domain are modified to 143  
144 produce a multivortex tornado (Zhao et al. 2021, 2023). In this study, 145  
146 the same cylindrical computational domain is applied to simulate a 147  
148 multivortex tornado, as shown in Fig. 1(a). The radius of the com- 4  
149 putational domain is  $R = 800$  m and the total height is 150  
151  $(h + L) = 1,100$  m. The inflow is simulated by the velocity-inlet on 152  
153 the side wall through the height of  $h$ . The outflow is set up on the 154  
155 top wall, which is considered as the pressure-outlet. A one-story, 156  
157 gable-roofed building is placed inside the computational domain 158  
159 and set up as a rigid body, as shown in Fig. 1(b). The length and 160  
161 width of the building are 20 and 10 m, respectively. The eave height 162  
163 is 5 m and the roof ridge height is 6.34 m. The orientation of this 164  
165 building with respect to the  $x$  direction is  $0^\circ$ , which means the long 166  
167 side of the building is parallel to the  $x$  direction. A transient, incom- 168  
169 pressible CFD simulation is conducted. 170

171 Haan et al. (2010) concluded that the vortex translating speed 172  
173 had a significant influence on the magnitude of wind loads acting 174  
175 on the building, finding that slow-moving vortices produced higher 176  
177 peak pressures and forces than fast-moving vortices. Therefore, it 178  
179 is necessary to include the tornado translation in the simulation 179  
180 in order to obtain the wind effects on structures more accurately. 180  
181 Considering the difficulty of moving the computation domain with 181  
182 a moving velocity-inlet, as shown in Fig. 1(c), the numerical simu- 182  
183 lation models the passage of a tornado over a stationary structure by 183  
184 introducing relative motion through a translating building beneath 184  
185 a stationary vortex. This approach has been widely adopted in both 185  
186 numerical and experimental studies to investigate tornado-structure 186  
187 interaction near the ground (Natarajan and Hangan 2012; Liu and 187  
188 Ishihara 2016; Li et al. 2019; Tang et al. 2018; Chen et al. 2023). 188  
189 While it does not capture the full three-dimensional tilt and asym- 189  
190 metry of a real tornado, it provides a practical method for resolving 190  
191 the near-surface aerodynamic effects that govern structural loading. 191  
192 To accommodate this, the computational domain is divided into 192  
193 several zones, with the zone including the building as “a rigid body 193  
194 zone.” The translation of civil structure is achieved by applying a 194  
195 constant moving speed on the rigid body zone and applying the 195  
196 layering dynamic mesh technique on the two zones before and 196  
197 after the rigid body zone along the long strip, which are treated as 197  
198 deforming zones, as shown in Fig. 2. In this way, the rigid body zone 198  
199 with the building translates through the two deforming zones and the 199  
200 deforming zones are adjusted automatically. The remaining zones 199  
201 on the bottom wall are set up as “moving wall” with the same speed 200  
202 in the same direction as the building to keep the relative movement 201  
203 to the ground. The upper zone is set up as a stationary domain. As 202  
204 to the translating speed, “the average translating speed of a tornado 203  
205 is 13.4 m/s but may vary from nearly stationary to 31.3 m/s,” 204  
206 reported by the National Severe Storms Laboratory (NSSL 1995). In 205  
207 this study, the translation speed is select as 15 m/s, which is close 206  
208 to the mean value. There are two stages in the simulation: stationary 207  
209 stage, which is the duration when the tornado does not translate, 208  
210 and translating stage, which is the duration of the tornado passing 209  
211 through the building. The center of the gable-roofed building is set 210  
212 up at  $x = 500$  m at first and then it translates along the  $x$  direction 211  
213 in the translating stage. 212

214 The mesh of the computational domain is developed in the 213  
215 software Pointwise and the hybrid mesh strategy is adopted. The 214  
216 structured hexahedral grid is adopted for almost all zones except the 215  
217 rigid body zone, as shown in Fig. 2(b), where unstructured mesh is 216  
218 applied. In the region near the ground surface and structural surface, 217  
219 where boundary layers are present, the grid inflation technique is 218  
220 applied to generate fine mesh. To be specific, 30 uniform boundary 219

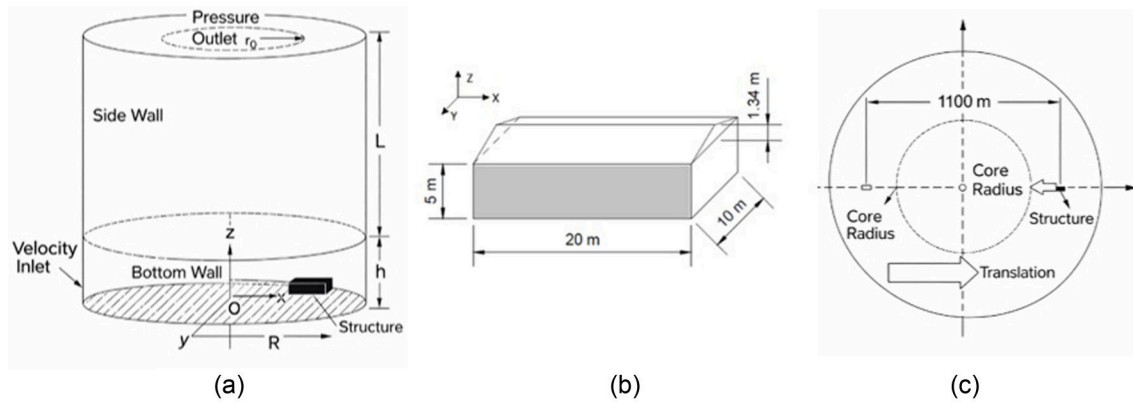


**Fig. 1.** Computational domain and sketch of a rectangular gable-roofed low-rise building: (a) computational domain; (b) sketch of gable-roofed building; and (c) tornado translation.

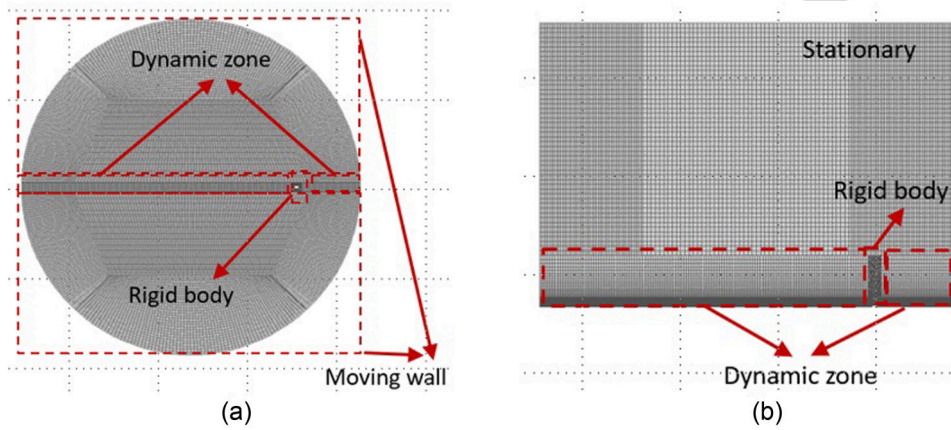


**Fig. 2.** Simulation setup of translation: (a) horizontal view; and (b) vertical view.

layers with a growth rate of 1.2 are added on the ground while another 30 smooth-transition boundary layers with a growth rate of 1.2 are added on the building surface to avoid a sudden change in grid size. Around the ground surface, the thickness of the first grid layer is 0.01 m and the  $y$  plus value is approximately 20; around the building surface, the thickness of the first layer is about 0.001 m and the  $y$  plus value is approximately 2. The total number of cells in each simulation is approximately 5 million.

In all these simulations, the governing equations of tornadic wind flow are filtered time-dependent Navier–Stokes equations. Assuming that momentum and mass are mainly transported by large eddies, the LES with the wall-adapting local eddy-viscosity (WALE,  $C_{wale} = 0.325$ ) subgrid model is adopted for turbulence modeling (Nicoud and Ducros 1999). In the LES, the segregated implicit solver is used to solve the governing equations with a semi-implicit method for pressure linked equation-consistent (SIMPLEC) method for pressure–velocity coupling, since the SIMPLEC scheme usually has a better convergence than pressure–implicit with splitting of operators (PISO) (Van Doornmaal and Raithby 1984; Hangan and Kim 2008). In addition, the simulation applies the least-squares-cell-based scheme for gradient, which is used to discretize the convection and diffusion terms in the flow conservation equations, the second-order discretization scheme for the pressure equation, and the bounded central differencing scheme for the momentum convection-diffusion equation (Anderson and Bonhaus 1994; Barth and Jespersen 1989; Leonard 1991). The bounded second-order implicit method with a time step of  $\Delta t = 0.02$  s is

used for time discretization in all cases for better stability. Standard sea-level atmospheric conditions [pressure = 101,325 N/m<sup>2</sup>, density = 1.225 kg/m<sup>3</sup>, temperature = 288.15 K, and dynamic viscosity = 1.789 × 10<sup>-5</sup> kg/(s \* m)] are adopted at the inlet and outlet and considered as the initial condition for the entire computational domain. A 400 s stationary analysis is performed first to generate a stable tornadic wind field while the structure is placed far away from the tornado core region. After the initial tornadic wind flow is generated, the building is set to move until it passes through the tornado core region.

The velocity inputs at the velocity inlet for all simulated cases are expressed by Eqs. (1)–(3) (Zhao et al. 2021), with the unit of meters per second (m/s) for velocity and the unit of meters (m) for vertical coordinate  $z$ . They represent the tangential, radial, and vertical velocity profiles along height, and they are applied on the velocity-inlet surface using a user define function (UDF). These velocity profiles are obtained based on the radar-measured data of the Spencer tornado

$$u_r = 20.3 \left( \frac{z}{20} \right)^{0.1816} \quad (1) \quad 245$$

$$u_r = \begin{cases} 49.26 \left( \frac{z}{20} \right)^{0.1736} - 81.37, & z \geq 20 \\ -32.11 \left( \frac{z}{20} \right)^{0.1429}, & z < 20 \end{cases} \quad (2) \quad 246$$

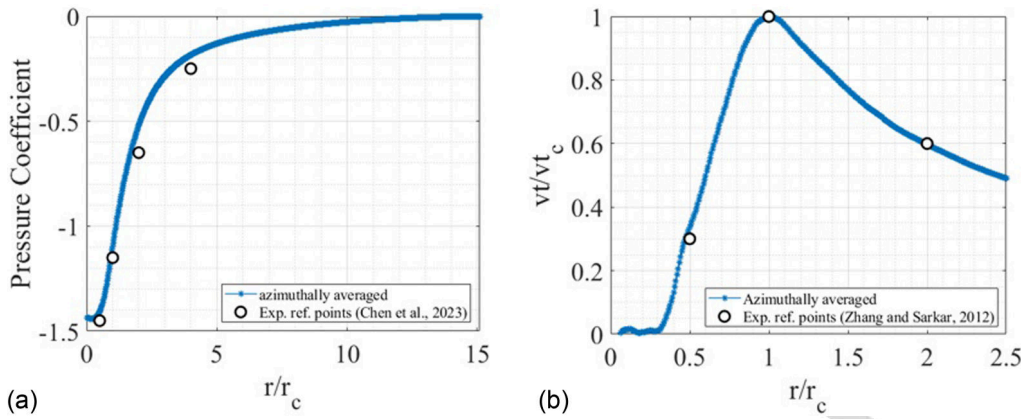


**Fig. 3.** Azimuthally averaged ground pressure coefficient and tangential velocity profiles: (a) ground pressure coefficient; and (b) tangential velocity.

$$u_w = \begin{cases} 8.84\left(\frac{z}{20}\right)^{-0.075} - 0.20\left(\frac{z}{20}\right)^{1.44} + 0.073z - 9.86, & z \geq 20 \\ -0.14\left(\frac{z}{20}\right)^{1.85} + 0.39\left(\frac{z}{20}\right)^{2.04}, & z < 20 \end{cases} \quad (3)$$

This simulation setup has been applied to simulate the Spencer tornado with a stationary condition that does not translate (Zhao et al. 2021). To further assess the simulation accuracy, the azimuthally averaged ground pressure coefficient ( $C_p$ ) distribution for the single-vortex tornado (Case 1) is compared with laboratory measurements reported by Tang et al. (2018) and Chen et al. (2023). In Fig. 3, the azimuthally averaged profiles are calculated by discretizing the horizontal plane into a polar grid with radial divisions from 0 m to 800 m in 1 m increments and tangential divisions from  $0^\circ$  to  $359^\circ$  in  $1^\circ$  increments. For each radial position, the tangential velocity was averaged over all azimuthal angles to obtain a representative circumferential mean profile as a function of radius. This approach smooths local fluctuations while preserving the characteristic vortex structure of each case. The present simulation captures a pronounced pressure deficit near the vortex core, with minimum  $C_p$  values reaching approximately  $-1.5$ . This trend and magnitude are highly consistent with the experimental results, where similar  $C_p$  deficits were observed beneath tornado-like vortices. The agreement between the numerical and laboratory profiles confirms the ability of the present CFD setup to reproduce realistic surface pressure characteristics under single-vortex conditions.

The azimuthally averaged tangential velocity profile from the multivortex simulation is compared to experimental particle image velocimetry (PIV) results by Zhang and Sarkar (2012). The normalized velocity profile ( $vt/vt_c$  versus  $r/r_c$ ) in the present study matches the PIV data closely, with  $vt/vt_c \approx 0.3$  at  $r/r_c = 0.5$  and  $vt/vt_c \approx 0.6$  at  $r/r_c = 2.0$ . This agreement confirms the fidelity of the simulated near-ground vortex structure in the multivortex case. Collectively, these comparisons demonstrate consistency between the present numerical results and prior experimental findings across vortex structure and pressure field, laying the solid foundation for the following analysis of wind loading.

### Tornadic Wind Fields with Different Flow Structures Simulated in This Study

In this study, tornadoes with four different flow structures are simulated, as given in Table 1. To be specific, three multivortex tornadoes and a single-vortex tornado are simulated. We consider swirl ratio and radial Reynolds number, two nondimensional parameters that

**Table 1.** Case setting and the tornado parameters

Case	$h$ (m)	$r_0$ (m)	$a$	$v$ (m/s)	$\omega$ (m/s)	$\tan\theta$	$r_c$ (m)	$S$	$Re_r$
1	300	300	1.00	20.3	32.11	0.632	53	0.316	$0.82 \times 10^9$
2	300	465	0.65	20.3	32.11	0.632	138	0.461	$0.82 \times 10^9$
3	200	550	0.36	20.3	32.11	0.632	200	0.878	$1.02 \times 10^9$
4	200	800	0.25	20.3	32.11	0.632	314	1.264	$1.02 \times 10^9$

control the flow structure; their definitions are reviewed here. Swirl ratio was first introduced by Ward (1972) for a laboratory tornado simulator and was expressed as

$$S = \frac{r_0 M}{2Q} = \frac{\tan\theta}{2a} \quad (4)$$

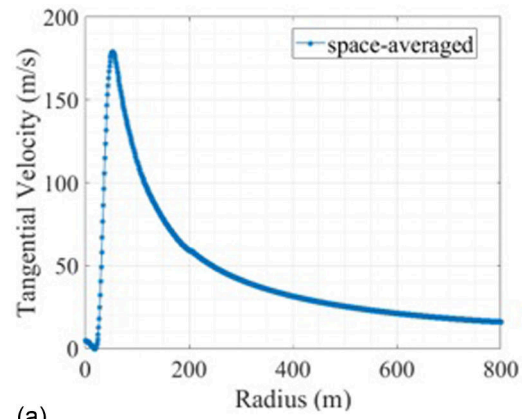
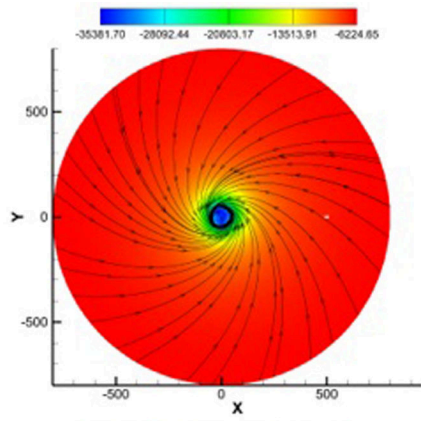
where  $Q$  = volume flow rate;  $M$  = circulation at the outer wall;  $r_0$  = radius of convergent area;  $a = h/r_0$ , which is also known as the aspect ratio;  $h$  = height of flow inlet; and  $\theta$  = angle of inflow to the radial direction at flow inlet. In this study, the second expression in Eq. (4) is adopted to calculate the swirl ratio of different simulated cases, because it is easy to change and control during initial setup. Herein,  $r_0$ ,  $h$ ,  $\theta$  are taken as the radius of the pressure outlet, the height of velocity inlet, and the inflow angle. Radial Reynolds number is defined as

$$Re_r = \frac{\rho Q}{\mu h} \quad (5)$$

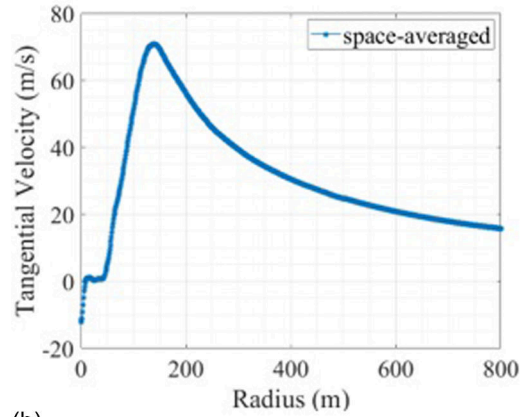
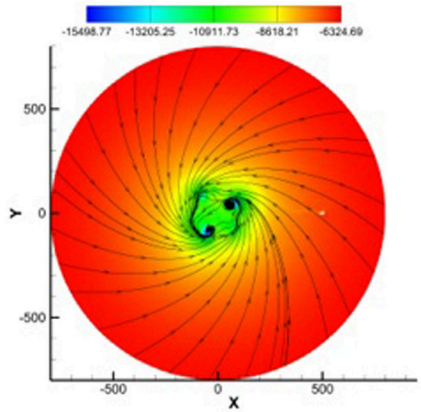
where  $\rho$  = density, and  $\mu$  = dynamic viscosity.

Previous studies have shown that increasing the swirl ratio can cause a tornado-like vortex to transition from a single-vortex structure to a multivortex structure (Ward 1972; Davies-Jones 1973; Church et al. 1979; Lewellen et al. 2000; Zhao et al. 2023). From Case 1 to Case 4, the swirl ratio is gradually increased to generate different tornado flow structures. The selected swirl ratios are based on the authors' previous studies (Zhao et al. 2021, 2023), which systematically examined the influence of swirl ratio and radial Reynolds number on vortex structure and wind characteristics in tornado-like flows. These studies identified characteristic thresholds associated with transitions between single-vortex and multivortex regimes.

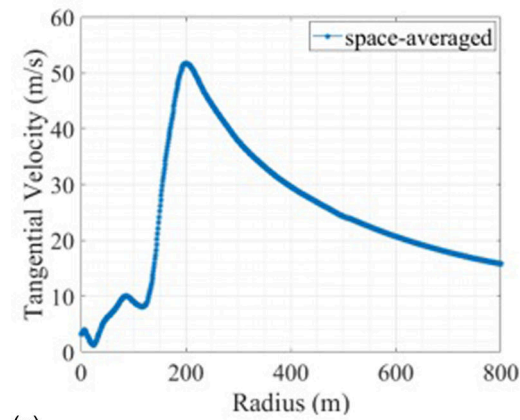
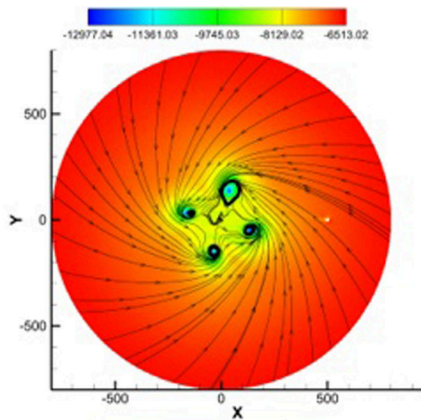
Four representative cases are considered in the present study. Case 1 represents a single-vortex tornado. Cases 2 and 3 represent



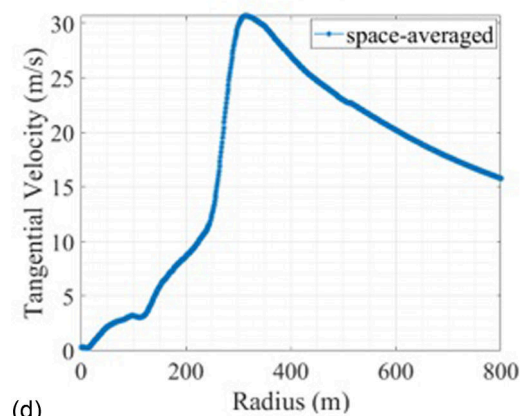
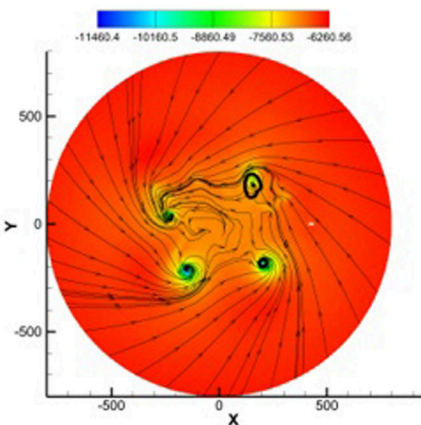
(a)



(b)



(c)



(d)

**Fig. 4.** Streamline, contour of static pressure and tangential velocity distribution on a horizontal plane of four simulated tornadoes: (a) Case 1; (b) Case 2; (c) Case 3; and (d) Case 4.

**Table 2.** Turbulence intensity at the core radius for different tornado flow structures

Case	$V_{hor\_mean}$	$V_{hor\_std}$	$TI_{hor}$	$V_{total\_mean}$	$V_{total\_std}$	$TI_{total}$
1	109.85	22.00	0.20	110.20	22.00	0.20
2	70.87	13.24	0.19	71.03	13.22	0.19
3	44.84	13.80	0.31	45.01	13.54	0.30
4	32.41	14.54	0.45	32.45	14.54	0.45

small multivortex tornadoes with two and four subvortices, respectively. Case 4 represents a larger multivortex tornado with four subvortices. This selection enables comparison across a range of swirl ratios associated with different vortex structures. The authors' previous stationary simulations, Case 2, with a swirl ratio of 0.461, produced a double-celled single-vortex structure near the threshold of vortex breakdown. In the present study, tornado translation is introduced through the moving ground and the civil structure. Under these conditions, the same swirl ratio results in the formation of two subvortices, indicating a transition to a multivortex tornado. This result is consistent with previous observations that tornado translation can locally increase the effective swirl ratio and promote multivortex breakdown (Diamond and Wilkins 1984).

Streamlines and pressure contours on a horizontal plane at a height of 5 m are shown in Fig. 4 to illustrate the resulting flow structures. In Case 1, a single vortex forms at the center of the computational domain, and the maximum pressure deficit occurs at the vortex center. In Cases 3 and 4, four subvortices are observed in the central region. These subvortices rotate about their own centers while orbiting within the larger vortex. The maximum pressure deficit occurs at the center of each subvortex rather than at the center of the overall vortex. In Case 2, two subvortices are observed within a smaller central region. These observations are consistent with the authors' previous findings (Zhao et al. 2021). The azimuthally averaged tangential velocity distributions along the radial direction on the same horizontal plane are also presented in Fig. 4. From Case 1 to Case 4, the core radius of the overall vortex increases, while the maximum tangential velocity decreases. For multivortex tornadoes, the core radius is defined as the radius at which the maximum azimuthally averaged tangential velocity occurs. The maximum velocity in each case is used to calculate the aerodynamic force and moment coefficients in the following section.

Turbulence intensity at the core radius in each case is evaluated using the instantaneous velocity records of the horizontal resultant speed  $V_{hor}$  and the total speed  $V_{total}$ . As summarized in Table 2, the single-vortex case (Case 1) exhibits a moderate turbulence intensity  $TI_{hor} = 0.2$ , while the turbulence intensity slightly decreases in Case 2 following the transition to a weak multivortex structure. With further increases in swirl ratio and more developed multivortex breakdown (Case 3), turbulence intensity increases significantly. The highest turbulence intensity is observed in Case 4, where  $TI_{hor}$  equals 0.45, indicating strong velocity fluctuations related to the reduced mean wind speed at the expanded core radius. Similar trends are observed for  $TI_{total}$ . For multivortex tornadoes, turbulence intensity increases with swirl ratio.

## Wind Effects of a Multivortex Tornado on a Low-Rise Building

### Total Forces/Moments Acting on the Entire Building

To quantify tornado-induced loading on the entire building, instantaneous force and moment coefficients are extracted as the building

translates across the tornado from one side to the other. The internal pressure is prescribed as the far-field absolute pressure at  $r = 800$  m and is held constant during the passage. This approach does not account for distributed leakage, transient pressurization effects, or other internal pressure dynamics; therefore, the net uplift coefficients reported here may be conservative. While the high uplift coefficients observed here are consistent with the potential for roof damage in tornado events, it should be noted that the lack of a discharge-based internal pressure model in this simulation may result in conservative estimates of uplift forces.

The total forces and moments exerted on the building are obtained by integrating the static pressure over the building envelope. Then, the force coefficients along the  $x$ ,  $y$ , and  $z$  axes [see Fig. 1(b)] and the moment coefficients about the three axes are calculated as follows:

$$CF_x = \frac{F_x}{\frac{1}{2}\rho V^2 S}, \quad CM_x = \frac{M_x}{\frac{1}{2}\rho V^2 S h} \quad (6) \quad 380$$

$$CF_y = \frac{F_y}{\frac{1}{2}\rho V^2 S}, \quad CM_y = \frac{M_y}{\frac{1}{2}\rho V^2 S h} \quad (7) \quad 381$$

$$CF_z = \frac{F_z}{\frac{1}{2}\rho V^2 S}, \quad CM_z = \frac{M_z}{\frac{1}{2}\rho V^2 S b} \quad (8) \quad 382$$

where  $F_x, F_y, F_z$  = total forces along the  $x, y, z$  axes,  $M_x, M_y, M_z$  = total moments about the  $x, y, z$  axes at the building center (see Fig. 1 for the direction of each axis),  $\rho$  = air density,  $V$  = reference velocity of each tornado,  $S$  = projected area normal to the  $y$  direction,  $h$  = height of roof ridge,  $b$  = longer dimensions of the building, and  $V$  = reference velocity. For a tornadic wind field, it is tricky to determine the averaging duration (e.g., 3 s, 1 s, or less) of wind velocity for reference velocity, as tornadic wind flow is highly transient, especially when the tornado translates. The averaging duration still remains an ongoing topic of discussion in the wind engineering and meteorological communities. To avoid the debate on the averaging duration, in this study, the azimuthally averaged tangential velocity at the radius where the maximum tangential velocity is obtained at the building eave height is the reference velocity.

Fig. 5 presents the force and moment coefficients versus the relative distance between the building and the tornado center. Positive distance denotes the approach side (building moving toward the center) and negative distance denotes the departure side; the same convention is used throughout Section 4. The two red vertical lines mark the core radius calculated estimated from the azimuthally averaged tangential velocity profile presented in Fig. 4. As shown in Fig. 5(a), as the building approaches the tornado center (the translating direction is from positive  $x$  to negative  $x$ ), the force coefficients gradually increase and reach the first peaks ( $CF_x = -0.56$  at  $x = 57.7$ ;  $CF_y = 1.51$  at  $x = 55.3$ ;  $CF_z = 4.01$  at  $x = 55.9$ ). After the building passes the core radius and approaches the tornado center, the absolute values of all three force coefficients decrease gradually with the decreasing relative distance to the tornado center. After the building passes the tornado center, these values switch to increase with increasing relative distance and reach the peaks when the building reaches the core radius on the other side of the tornado ( $CF_x = 0.63$  at  $x = -61.9$ ;  $CF_y = -1.22$  at  $x = -65.2$ ;  $CF_z = 3.46$  at  $x = -63.1$ ). The sign reversal of  $CF_x$  indicates that the net horizontal force component is directed toward the tornado center on each side of the path, while  $CF_y$  reverses consistently with the tangential flow direction of the counterclockwise

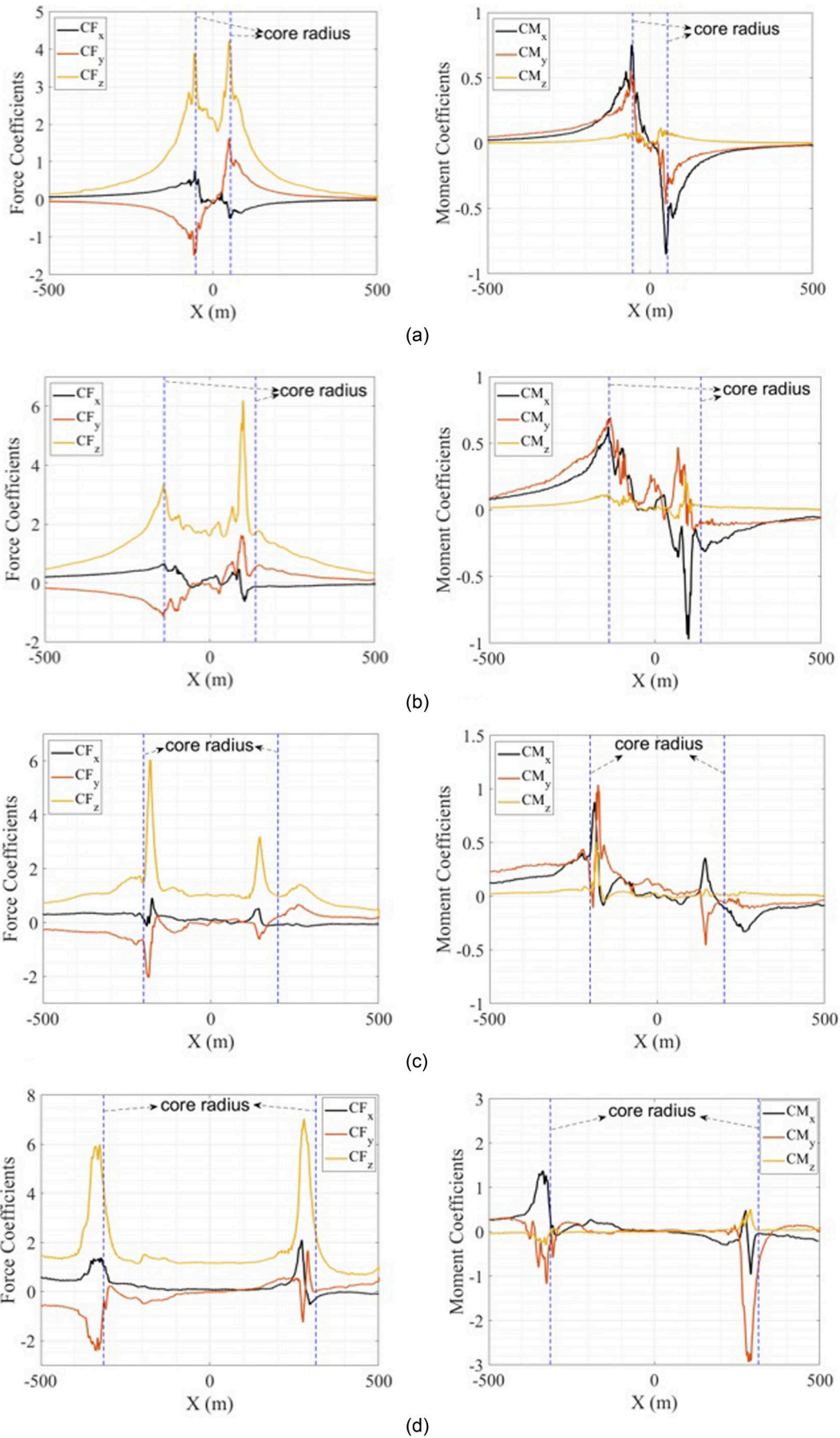


**Fig. 5.** Coefficients of forces and moments acting on the low-rise building induced by the four different tornadoes: (a) Case 1; (b) Case 2; (c) Case 3; and (d) Case 4.

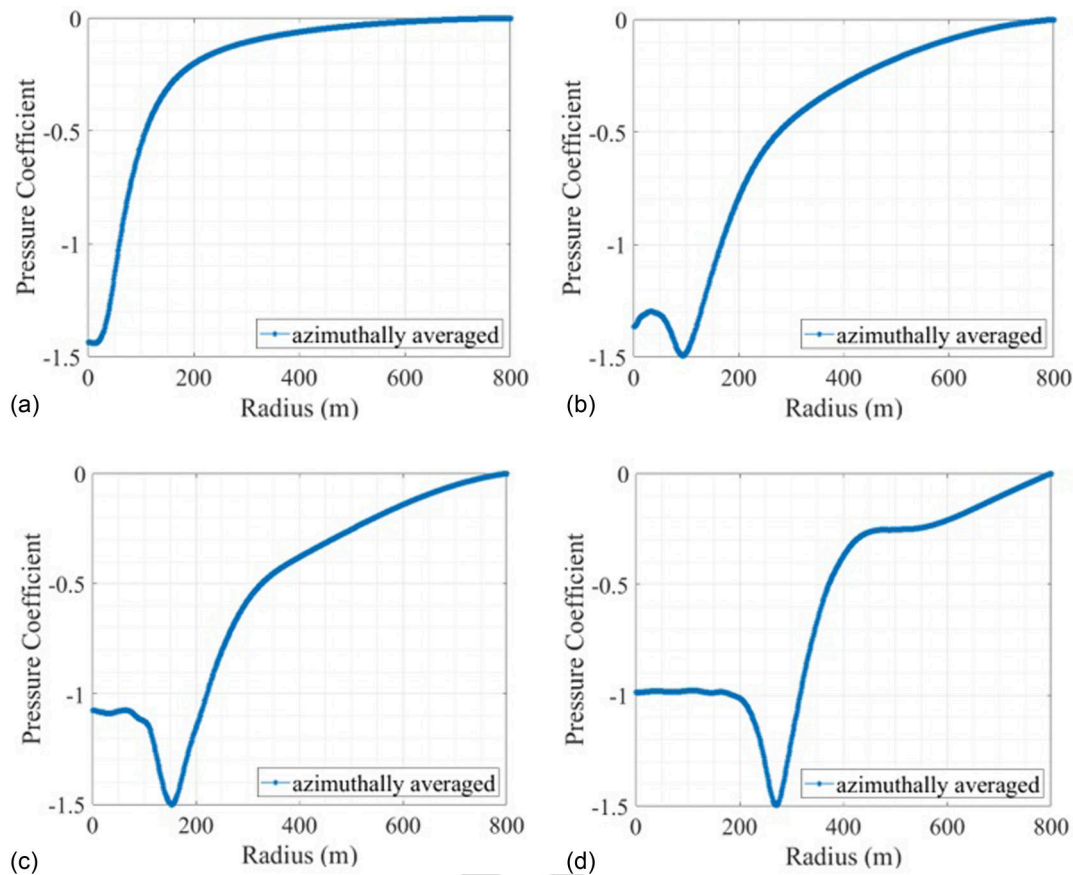


Fig. 6. Azimuthally averaged pressure coefficient profiles as a function of radial distance: (a) Case 1; (b) Case 2; (c) Case 3; and (d) Case 4.

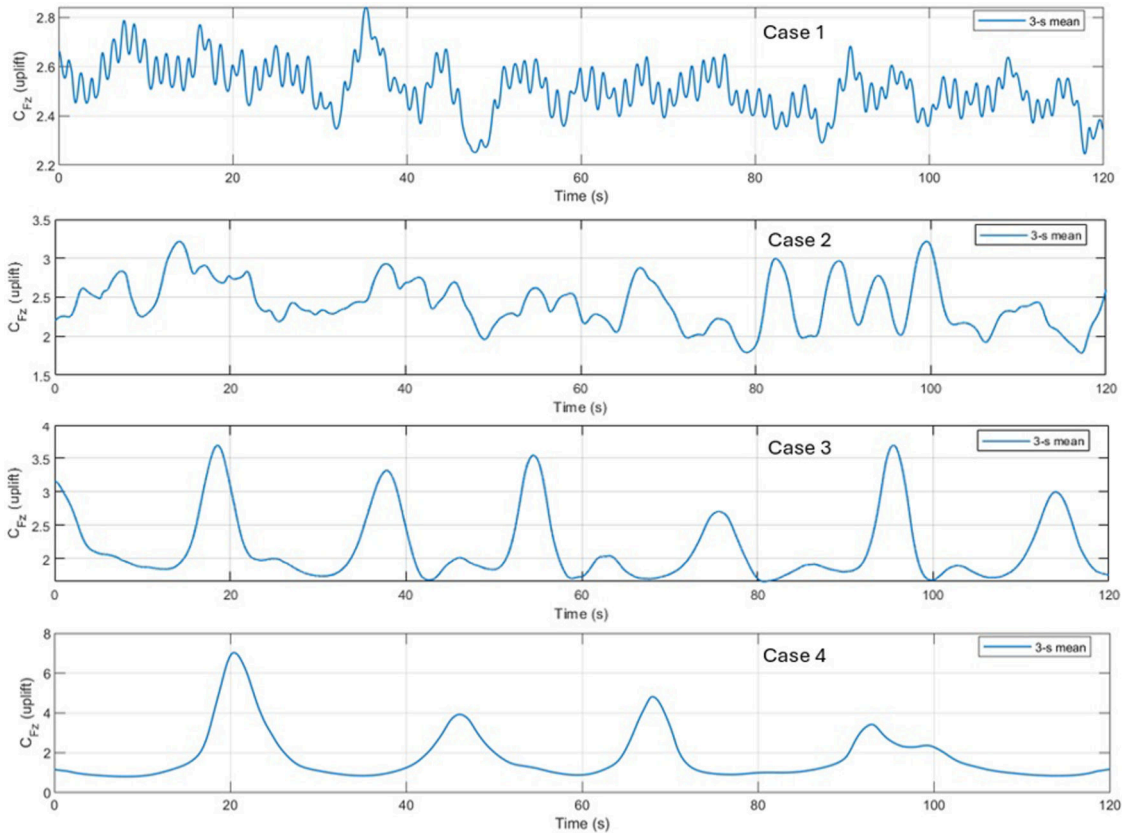
vortex (Northern Hemisphere). Between 129.1 and  $-139.8$  m (about 5.4 times of core radius),  $CF_z$  remains positive (pointing upward, along the positive  $z$  direction), reflecting sustained roof suction from both the tornado pressure deficit and aerodynamic effects. The obtained peak value of  $CF_z$  is consistent with the reported experimental results (Haan et al. 2010; Chen et al. 2023). Uplift dominates the net loading, consistent with roof failure being a common tornado damage mechanism and contrasting with straight-line winds where along-wind drag typically governs (Bluestein and Golden 1993; Karstens et al. 2013).

Fig. 5(b) shows that the overturning moments  $CM_x$  and  $CM_y$  vary similarly to  $CF_y$  and  $CF_x$ , respectively, because overturning moments are driven primarily by the corresponding horizontal forces. Both moments change signs as the building crosses the vortex center, which indicates that the applied wind loads tend to cause the building to overturn toward the tornado center. The torsional moment coefficient  $CM_z$  is negligible in Case 1 because the surface pressure field is nearly symmetric. Consistent with the force results, the largest moment coefficients also occur near the core radius.

Figs. 5(c-h) show that the multivortex cases follow the same overall dependence on distance but with markedly more intermittent loading. Two groups of peaks occur, indicating sequential encounters with two subvortices as they orbit within the overall vortex. Each peak group resembles the Case 1 signature (including sign changes of  $CF_x$  and  $CF_y$  as the building crosses a vortex center) but is compressed in distance and duration because the subvortex core is much smaller (e.g., Case 4 compared with Case 1). Between the two peak groups, the coefficients remain small even though the building is within the core of the overall vortex. To clarify this observation, Fig. 6 presents the azimuthally averaged pressure

coefficient profiles as a function of radial distance for each case. In Case 1, the pressure coefficient decreases continuously toward the tornado center, reaching its minimum at the vortex center. By contrast, in multivortex tornado cases, the minimum pressure coefficient occurs at an intermediate radius corresponding to the location of the subvortex center, and the pressure near the center of the overall vortex is relatively higher. This pattern indicates that the most severe local suction forces in a civil structure are governed by the proximity of a subvortex core rather than by the overall vortex center. In addition, multivortex tornadoes also amplify peak loads: the peak uplift coefficients in Cases 2–4 are approximately 1.54, 1.50, and 1.75 times those in Case 1, and  $CF_{z,max}$  exceeds 6 in all multivortex cases.

Fig. 7 presents the 3 s averaged uplift coefficient time histories obtained from stationary simulations with the building fixed at the tornado core radius for Cases 1–4. In the single-vortex case (Case 1), the peak 3 s averaged uplift coefficient is relatively modest, about 2.84, reflecting a relatively steady loading environment dominated by the main vortex core. In contrast, the multivortex cases exhibit substantially larger peak 3 s averaged uplift coefficients associated with the repeated passage of subvortices near the building. For Cases 2 and 3, the peak 3 s averaged uplift coefficients increase to 3.21 and 3.68, respectively, but the lowest ones also decrease below 2, indicating transient load amplification as individual subvortices interact with the building. Case 4 produces the largest uplift coefficient, with a peak of 7.03, more than twice that of the single-vortex case. The increase in the peak 3 s averaged uplift coefficients from Case 1 to Case 4 further demonstrates that higher swirl ratios and more developed multivortex structures intensify uplift loads on the building. It is noted that in multivortex tornadoes, the rotation of subvortices around the tornado center, their relative location with



**Fig. 7.** Time histories of 3 s averaged uplift coefficient at the tornado core radius. (Note: The spikes in the last two figures indicate when a subvortex passes the measurement point.)

respect to the building, as well as their own unstable and varying structure introduce strong uncertainties in the loading process, making it challenging to quantify the impact of a multivortex tornado on the building.

What causes the significant increase in the magnitude of the peak values of  $CF_z$  under the multivortex tornado? This can be explained by the unique characteristics of wind flow in multivortex tornadoes. Inside a multivortex tornado, each subvortex not only rotates around its own center but also swirls along the core radius of the overall vortex. The significant atmospheric pressure drop does not occur at the center of the overall vortex; instead, it occurs at the center of each subvortex, which is very close to the location of the maximum wind speed (at the core radius of the subvortex). These two locations are very close to each other due to the small size of a subvortex. Accordingly, when the subvortex attacks the building, the action on the building should be the superposition of the maximum negative pressure due to atmospheric pressure drop and the aerodynamic force due to the maximum wind speed. On the contrary, in the single-vortex tornado, the significant atmospheric pressure drop occurs at the tornado center, while the aerodynamic force due to the maximum wind speed occurs at the core radius. These two locations are relatively far away from each other and thus the superposition may not be that important.

It should be noted that despite lower peak values, the total wind load impulse (time-integrated force) in the single-vortex tornado may be comparable to or even exceed that of multivortex tornadoes. This is due to the sustained high  $CF_z$  values across the entire core region in single-vortex tornadoes, compared to the more intermittent, localized peaks in multivortex cases. Furthermore, the selection of appropriate reference velocity becomes particularly

critical when evaluating multivortex tornadoes, since they exhibit significant spatial and temporal velocity fluctuations due to the presence of subvortices. This velocity variability poses challenges for calculating normalized force coefficients that accurately represent the wind loading effects.

### Pressure Distribution on Building Surface and Flow Field around Building

To link the global force coefficients to local flow features, surface pressure and surrounding flow fields are examined at the instant of peak uplift ( $CF_{z,max}$ ) in each case. Fig. 8 presents surface pressure coefficient distribution on the building, while Figs. 9 and 10 show horizontal-plane velocity magnitude and pressure coefficient contours with streamlines at  $z = 2$  m. Fig. 11 presents the corresponding vertical flow structure on the  $xz$  plane ( $y = 0$  m). The pressure coefficient is defined as

$$C_p = \frac{p - p_\infty}{\frac{1}{2}\rho V^2} \quad (9)$$

where  $C_p$  = pressure coefficient,  $p$  = static pressure, and  $p_\infty$  = environmental pressure at the radius of 800 m.

Fig. 8 presents a substantial increase in both the magnitude and the spatial range of surface pressure coefficients at the instant of peak uplift. In the single-vortex case (Case 1), the surface pressure coefficient varies from approximately  $C_{p,min} = -2.44$  to  $C_{p,max} = 0.72$  ( $\Delta C_p = 3.16$ ). In contrast, the multivortex cases exhibit much stronger suction and larger pressure gradients: Case

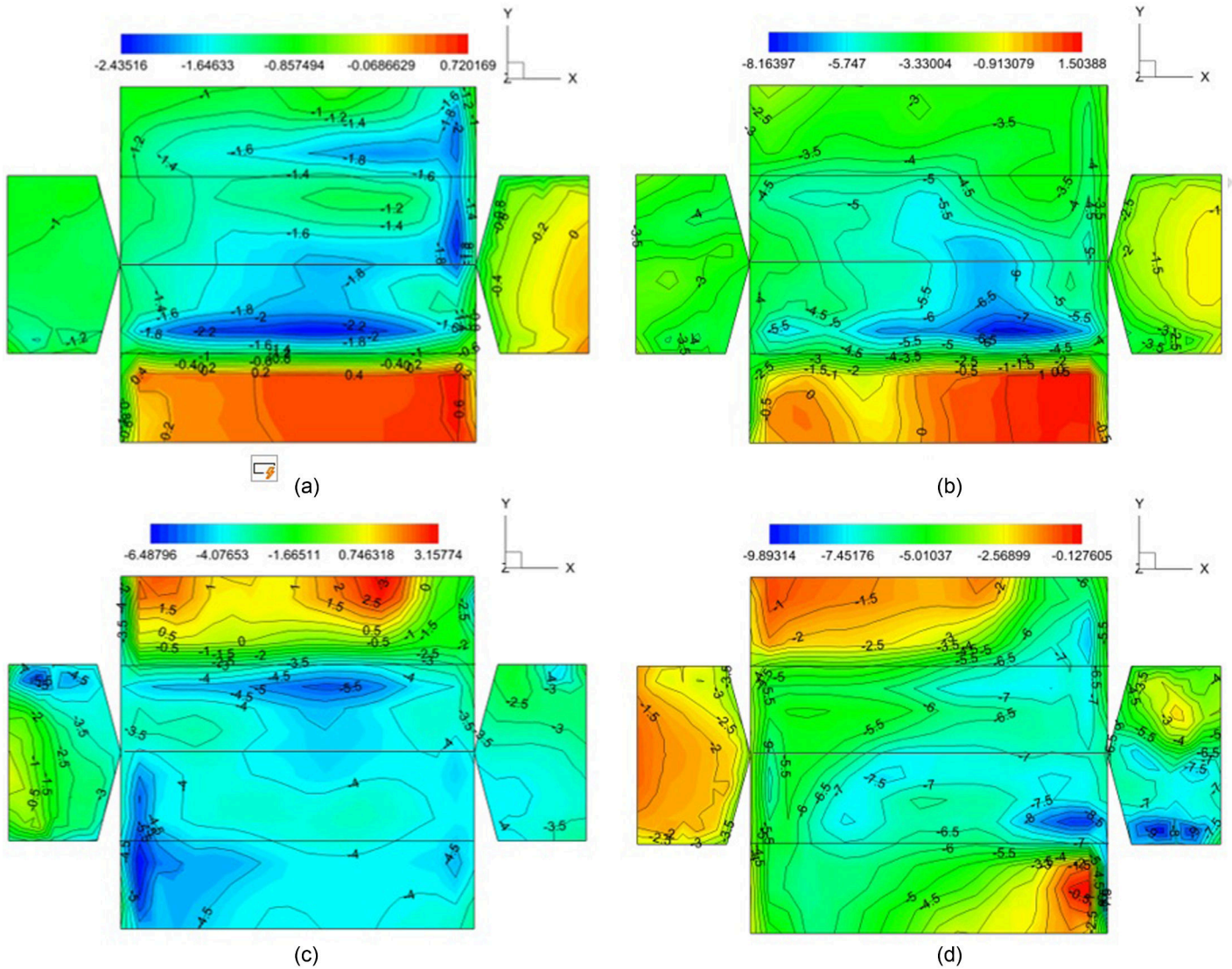


**Fig. 8.** Pressure coefficients on the low-rise building induced by the four different tornadoes: (a) Case 1; (b) Case 2; (c) Case 3; and (d) Case 4.

2 reaches  $C_{p,\min} = -8.16$  and  $C_{p,\max} = 1.50$  ( $\Delta C_p = 9.67$ ), Case 3 reaches  $C_{p,\min} = -6.49$  and  $C_{p,\max} = 3.16$  ( $\Delta C_p = 9.65$ ), and Case 4 reaches  $C_{p,\min} = -9.89$  with  $C_{p,\max} = -0.13$  ( $\Delta C_p = 9.77$ ). Relative to Case 1, the maximum suction intensifies by factors of approximately 3.35 (Case 2), 2.66 (Case 3), and 4.06 (Case 4). Notably, at the peak-uplift instant in Case 4, the entire building envelope remains under suction ( $C_{p,\max} < 0$ ), indicating that positive stagnation pressures are suppressed and the loading is dominated by the tornado pressure deficit and localized subvortex-induced suction. These quantitative differences in surface pressure magnitude are consistent with the larger uplift coefficients reported in Section 4.1 for the multivortex tornadoes. In the single-vortex tornado (Case 1), the roof is dominated by negative pressure (suction), with the largest magnitudes near roof edges [Fig. 8(a)]. The windward lower wall exhibits positive pressure from the approaching flow, while the leeward wall and roof exhibit suction due to separation and the large-scale tornado pressure deficit [Figs. 9(a) and 10(a)]. This pressure pattern produces a net horizontal force aligned with the tangential flow ( $CF_y$ ) and directed toward the vortex center ( $CF_x$ ), and a dominant uplift force ( $CF_z$ ).

In the multivortex cases, the pressure field becomes less symmetric and more localized. Suction patches concentrate on limited

roof areas and on one sidewall when a subvortex core passes near the building [Figs. 8(b–d)], which contributes to the sharp peaks observed in the profile of force coefficients. Case 2 retains a pattern similar to Case 1 but with reduced symmetry. In Cases 3 and 4, localized pressure deficits associated with the subvortex core and the strongly unsteady near-ground flow produce substantial differences between opposite faces. Because tangential velocity reverses on the inner side of a subvortex, the approaching flow can appear on different faces depending on the instantaneous subvortex position [Figs. 9(b–d)]. As a result, windward and leeward regions shift rapidly and the net horizontal force tends to align toward the local subvortex center, consistent with the sign changes of  $CF_x$  and  $CF_y$ . For larger subvortices (Case 4), the strong background pressure deficit and accelerated near-wall flow reduce positive windward pressures and can render them negative.

To quantify the relative roles of the tornado (or subvortex) pressure deficit and the local aerodynamic response of the building, the minimum surface pressure coefficient is decomposed as  $C_p = C_{p,\text{deficit}} + C_{p,\text{dyn}}$ , where  $C_{p,\text{deficit}}$  is estimated from the pressure coefficient in the flow field immediately surrounding the building, and  $C_{p,\text{dyn}}$  represents the remaining contribution associated with local flow acceleration and separation. Using

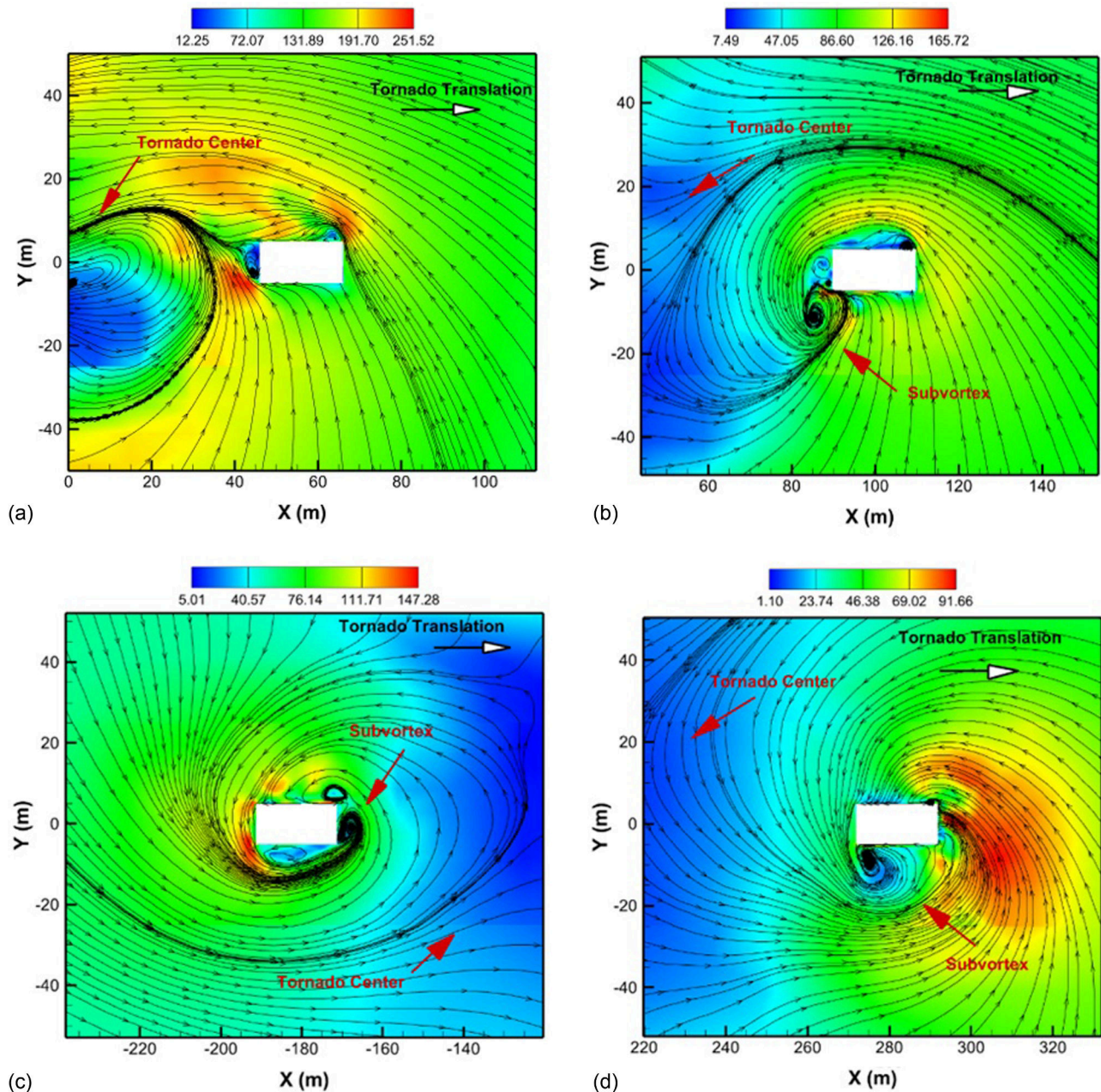


**Fig. 9.** Resultant velocity contour with streamlines around the building at the elevation of 2 m in four different tornadoes (horizontal view): (a) Case 1; (b) Case 2; (c) Case 3; and (d) Case 4.

580  $C_{p,deficit} = -0.60, -2.03, -5.36,$  and  $-6.20$  for Cases 1–4, respec- 595  
 581 tively, and the corresponding minimum surface pressure  $C_p$  (maxi- 596  
 582 mum absolute value) from Fig. 8, the pressure-deficit contribution 597  
 583 accounts for approximately 25% of the peak suction in Cases 1 and 2 598  
 584 but increases to 83% in Case 3 and 63% in Case 4. These results indi- 599  
 585 cate that peak suctions in the multivortex cases are increasingly gov- 600  
 586 erned by the localized pressure deficit of a nearby subvortex core, 601  
 587 whereas in the single-vortex and transitional cases a large frac- 602  
 588 tion of the suction is produced by the local aerodynamic response driven 603  
 589 by the near-wall velocity field. This decomposition is approximate 604  
 590 because the “dynamic” term aggregates both velocity-driven pres- 605  
 591 sure changes and building-induced flow separation; nevertheless, it 606  
 592 provides a quantitative measure of how the governing mechanism 607  
 593 shifts from wind-driven suction to subvortex-core deficit as the flow 608  
 594 transitions to multivortex structure. 609

As shown in Fig. 11, the vertical flow structure also differs 595  
 between the single-vortex and multivortex cases. In Case 1, inflow 596  
 from the inner and outer regions converges above the building and 597  
 forms a coherent updraft over the roof. In the multivortex cases, the 598  
 flow is influenced by subvortex circulation and exhibits more com- 599  
 plex vertical motion. With increasing swirl ratio, the outer-region 600  
 inflow weakens relative to the near-core flow, and the combined 601  
 local flow near the building becomes more outward directed; Case 602  
 4 shows pronounced redirection of the near-roof flow, including 603  
 backward and upward motion. Consistent with these observations, 604  
 peak velocities occur mainly near the roof in Case 1 but shift toward 605  
 the sidewalls in the multivortex cases. These differences imply 606  
 distinct mechanisms for roof suction. In the single-vortex case, 607  
 negative roof pressures arise primarily from large-scale acceleration 608  
 and separation over the roof. In the multivortex cases, negative 609

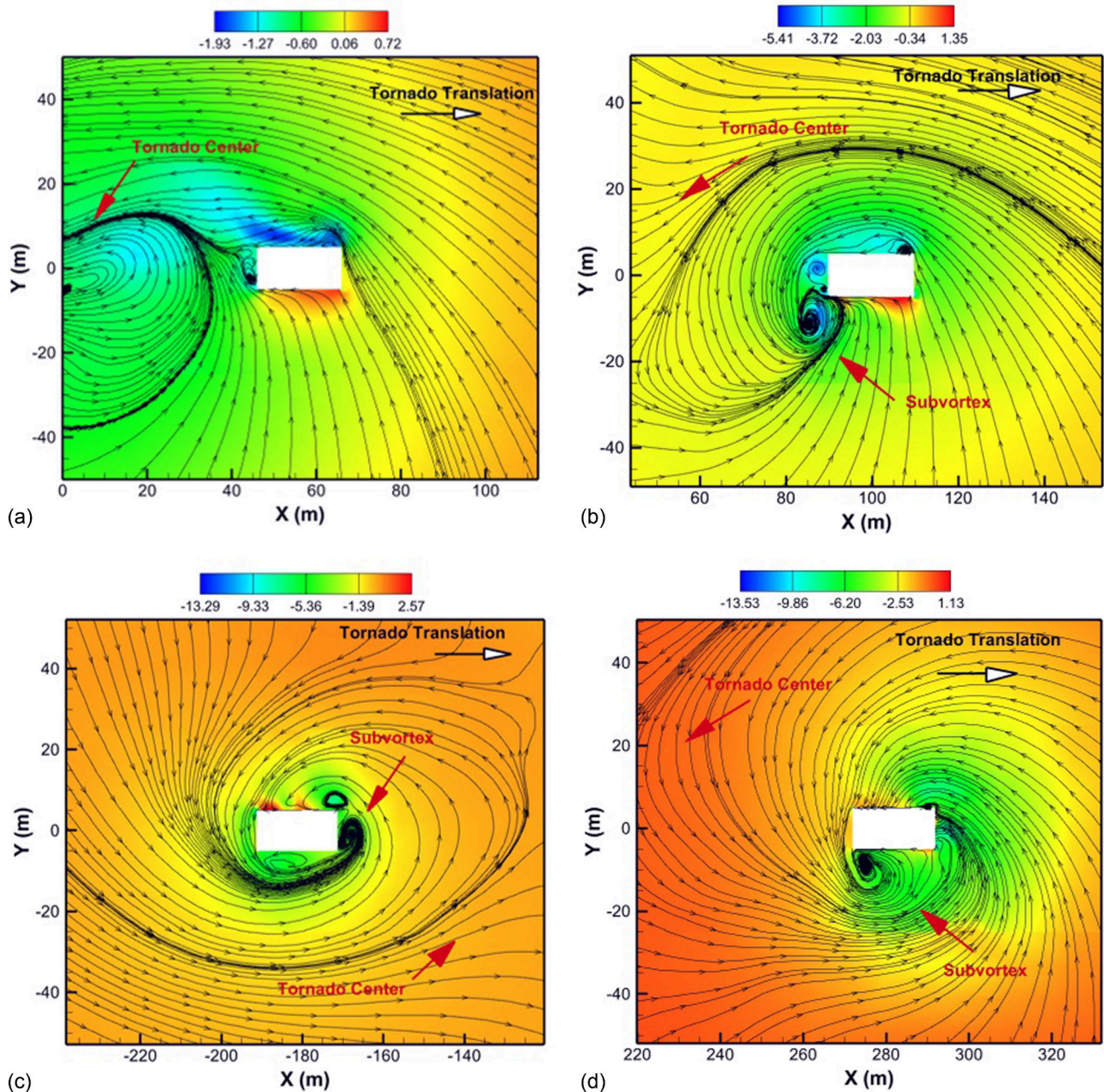


**Fig. 10.** Pressure coefficient contour around the building at the elevation of 2 m in four different tornadoes: (a) Case 1; (b) Case 2; (c) Case 3; and (d) Case 4.

610 roof pressures reflect a combination of near-wall acceleration, and  
 611 the intense pressure deficit within subvortex cores. Together, these  
 612 effects explain the larger peak uplift coefficients and increased  
 613 variability observed for the multivortex tornadoes.

614 **Effect of Angle of Attack on Aerodynamic Forces**  
 615 **and Moments**

616 To investigate the influence of building orientation on tornado-  
 617 induced aerodynamic loading, more cases with a range of angles  
 618 of attack (AOA) are simulated. Unlike the translating cases used in  
 619 the previous sections, a stationary tornado configuration is adopted  
 620 for the angle-of-attack analysis in order to isolate the influence  
 621 of building orientation from the influence of tornado translation.  
 622 The analysis is conducted for a representative multivortex case,

Case 3, with the building placed at the core radius of the overall  
 vortex, where strong velocity gradients and intermittent loading  
 are expected. The AOA is defined as the counterclockwise rotation  
 of the building from the global  $x$  axis, with  $0^\circ$  corresponding to  
 alignment of the building's long side with the  $x$ -direction. The AOA  
 is varied from  $-75^\circ$  to  $+90^\circ$  in  $15^\circ$  increments. For each orientation,  
 time histories of aerodynamic forces and moments are obtained  
 over a total duration of 180 s, and the first 60 s are discarded  
 to remove initial transients. All statistical metrics are evaluated  
 over the remaining 120 s. The force and moment coefficients are  
 computed using the definitions given in Eqs. (6)–(8).

Fig. 12 presents the variation of the uplift coefficient  $C_{F_z}$  with  
 AOA, where three metrics are shown for each orientation: the  
 instantaneous maximum value, the 99th percentile, and the peak  
 value of the 3 s moving-average time history of  $C_{F_z}$ . The results

623  
624  
625  
626  
627  
628  
629  
630  
631  
632  
633  
634  
635  
636  
637

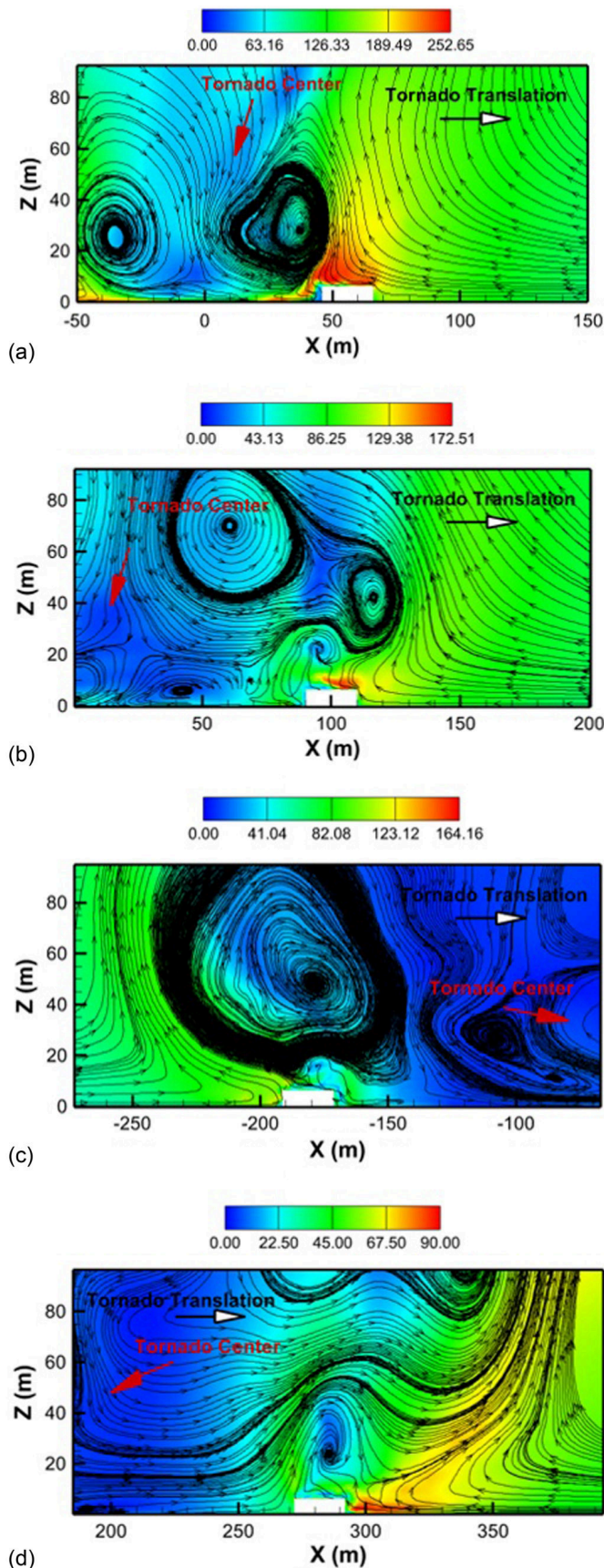


Fig. 11. Wind flow structures around the low-rise building in four different tornadoes (vertical view): (a) Case 1; (b) Case 2; (c) Case 3; and (d) Case 4.

suggest that  $C_{F_z}$  is strongly dependent on building orientation. All three metrics exhibit a consistent variation trend with AOA and reach their maximum values at approximately  $+15^\circ$ , demonstrating that the governing orientation for uplift is robust and not sensitive to the choice of metric. The instantaneous maximum values are consistently much higher than the corresponding percentile-based and duration-averaged metrics, reflecting the presence of short-duration extreme events.

Fig. 13 shows the corresponding variation of the torsional moment coefficient  $C_{M_z}$  with AOA. In contrast to  $C_{F_z}$ ,  $C_{M_z}$  exhibits a markedly different AOA. The largest  $C_{M_z}$  values occur at negative AOA, with peak values observed near  $-60^\circ$ , depending on the metric considered. The instantaneous maximum  $C_{M_z}$  show particularly strong sensitivity to AOA, while the 99th percentile and 3 s peak metrics show that the observed trend is not dominated by a single isolated spike. These results demonstrate that the AOA producing the maximum torsional response does not coincide with that producing the maximum uplift response, indicating that different structural limit states may govern at different orientations under tornado loading.

To illustrate the transient nature of the aerodynamic loading and to provide physical context for the statistical metrics, Fig. 14 presents time histories of the uplift and torsional moment coefficients of a representative case (an AOA of  $0^\circ$ ). Both coefficients exhibit intermittent, short-duration peaks superimposed on a lower background level. These fluctuations are attributed to the passage of subvortices relative to the translating tornado core, which locally intensifies the pressure and velocity fields around the civil structure. Such intermittent events contribute to the instantaneous peak coefficients and explain the observed differences between instantaneous, percentile-based, and duration-averaged metrics. The time-history behavior further supports the need to consider multiple metrics when evaluating angle-of-attack effects in tornado-induced loading.

Overall, the results demonstrate that building orientation plays a critical role in determining both the magnitude and the governing mode of aerodynamic loading in tornado wind fields. While uplift and torsion are both strongly affected by angle of attack, they reach their peaks at different orientations, underscoring the importance of considering a range of angles when assessing tornado-induced wind loading.

### Conclusions

This study examines the wind effects induced by a multivortex tornado acting on a low-rise building using large-eddy simulations. One single-vortex tornado and three multivortex tornadoes with increasing swirl ratios are investigated. The results show that multivortex tornadoes produce wind effects that are fundamentally different from those induced by a single-vortex tornado. For the multivortex tornadoes, the building experienced multiple distinct peaks in uplift and horizontal forces as individual subvortices passed nearby, whereas the single-vortex tornado produced a smoother and more spatially distributed loading pattern. Along the translating path, peak uplift coefficients in the multivortex cases increase by approximately 1.5–1.75 relative to the single-vortex case, demonstrating clear amplification associated with subvortex interactions. Meanwhile, the continuous rotation of subvortices around the tornado center causes very high turbulence intensity near the core radius and their relative motion with respect to the building introduces strong nonstationariness, making it difficult to characterize multivortex tornado impacts.

Analysis of surface pressure distributions reveals a pronounced shift in the governing suction mechanism with tornado structure.

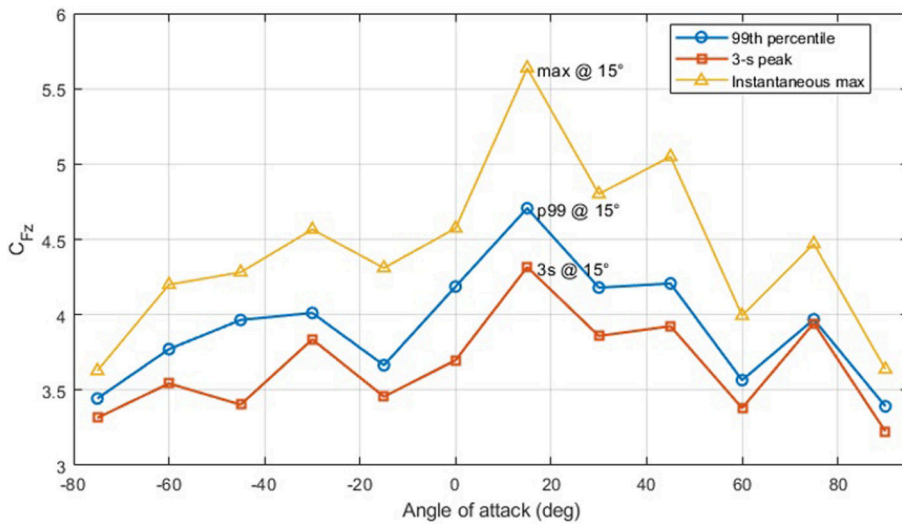


Fig. 12. Effect of angle of attack on uplift coefficient  $C_{Fz}$ .

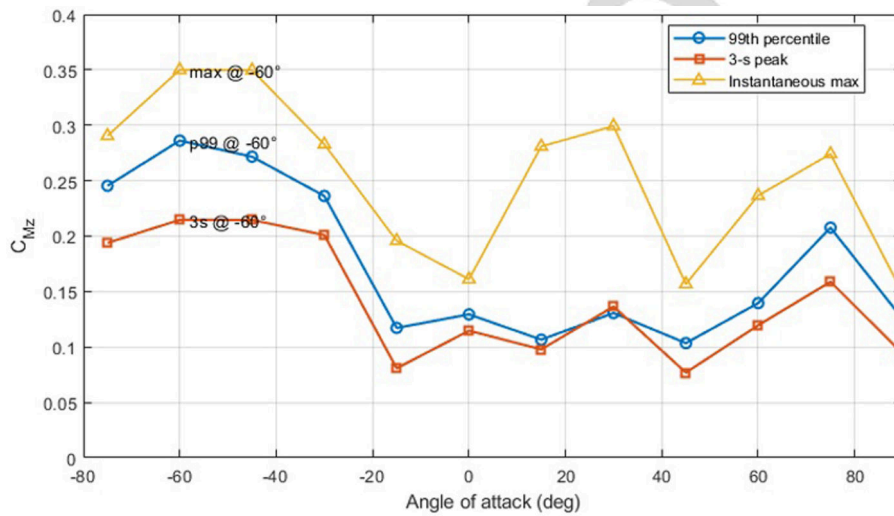


Fig. 13. Effect of angle of attack on torsional moment coefficient  $C_{Mz}$ .

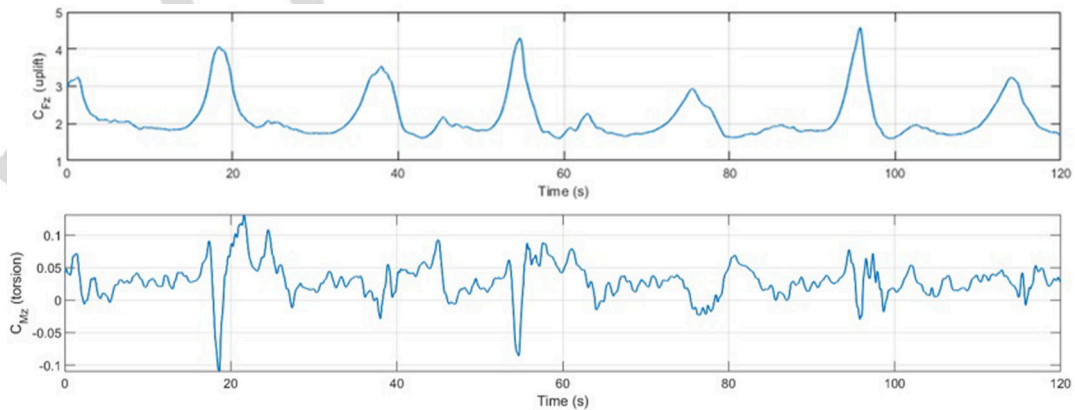


Fig. 14. Representative time histories of uplift and torsional moment coefficients at  $0^\circ$  angle of attack.

698 In the single-vortex tornado, a large portion of roof suction is  
 699 associated with local aerodynamic effects driven by near-wall flow  
 700 acceleration. In contrast, in the multivortex cases, peak suction  
 701 is dominated by the intense pressure deficit within the subvortex

cores, leading to stronger and more spatially concentrated negative  
 pressures. In the largest multivortex case (with the highest swirl  
 ratio), the entire building envelope remained under suction at the  
 peak-uplift instant. In addition, the angle-of-attack analysis further

702  
 703  
 704  
 705

706 shows that the building orientation affects wind effects significantly  
 707 in the multivortex case, and that the orientations producing the  
 708 maximum uplift and the maximum torsion do not coincide.  
 709 Overall, the simulation results demonstrate that subvortex flow  
 710 structure plays a critical role in governing wind effects on low-rise  
 711 buildings. The reported peak values should be interpreted as mechan-  
 712 istic indicators of potential load amplification associated with a  
 713 subvortex attacking the building. A multivortex tornado's potential  
 714 to generate more severe and complex loading conditions than the  
 715 single-vortex tornado suggests the need for future studies to explic-  
 716 itly account for multivortex tornado dynamics when characterizing  
 717 tornado-induced wind effects.

## 718 Limitations and Future Work

719 While the relative-motion approach adopted in this study provides  
 720 a practical and validated framework for examining tornadic wind  
 721 effects on low-rise buildings, it has several inherent limitations. By  
 722 translating the building beneath a stationary tornado-like vortex,  
 723 the simulation captures the relative passage of the tornado near the  
 724 ground but does not account for possible tilt of the tornado core,  
 725 asymmetric inflow associated with the parent storm, or vertical  
 726 evolution of the vortex during translation. These effects may alter  
 727 the flow field at higher elevations and influence load distributions on  
 728 tall structures.

729 Accordingly, the present modeling approach is most appropriate  
 730 for low-rise buildings, where near-ground wind fields and localized  
 731 vortex–structure interactions govern loading behavior. Extension of  
 732 this approach to high-rise buildings would require explicit modeling  
 733 of a fully translating and potentially tilted tornado vortex.

## 734 Data Availability Statement

735 <sup>10</sup> Some or all data, models, or code that support the findings of this  
 736 study are available from the corresponding author upon reasonable  
 737 request.

## 738 Acknowledgments

739 The authors greatly appreciate the financial support from the  
 740 VORTEX-SE Program within the NOAA/OAR Office of Weather  
 741 and Air Quality under Grant No. NA20OAR4590452. The authors  
 742 also greatly appreciate the financial support from National Science  
 743 Foundation, through the project “Damage and Instability Detection  
 744 of Civil Large-scale Space Structures under Operational and Multi-  
 745 hazard Environments” (Award No. 1455709).

## 746 Author Contributions

747 Yi Zhao: Conceptualization; Data curation; Software; Validation;  
 748 Visualization; Writing – original draft; Writing – review and edit-  
 749 ing. Guirong Yan: Conceptualization; Supervision; Writing – orig-  
 750 inal draft; Writing – review and editing. Tetsuya Takemi: Writing –  
 751 review and editing. John van de Lindt: Writing – review and editing.

## 752 References

753 Agee, E. M., J. T. Snow, and P. R. Clare. 1976. “Multiple vortex fea-  
 754 tures in the tornado cyclone and the occurrence of tornado families.”  
 755 *Mon. Weather Rev.* 104 (5): 552–563. [https://doi.org/10.1175/1520-0493\(1976\)104<0552:MVFITT>2.0.CO;2](https://doi.org/10.1175/1520-0493(1976)104<0552:MVFITT>2.0.CO;2).

Anderson, W. K., and D. L. Bonhaus. 1994. “An implicit 757  
 upwind algorithm for computing turbulent flows on unstructured 758  
 grids.” *Comput. Fluids* 23 (1): 1–21. [https://doi.org/10.1016/0045-7930\(94\)90023-X](https://doi.org/10.1016/0045-7930(94)90023-X). 759  
 760  
 Barth, T., and D. Jespersen. 1989. “The design and application of 761  
 upwind schemes on unstructured meshes.” In *Proc., 27th Aero- 762  
 space Sciences Meeting, AIAA-89-0366*. [https://doi.org/10.2514/6. 763  
 .1989-366](https://doi.org/10.2514/6.1989-366). <sup>11</sup> 764  
 Bienkiewicz, B., and P. Dudhia. 1993. “Physical modeling of tornado-like 765  
 flow and tornado effects on building loading.” In *Proc., 7th US 766  
 National Conf. on Wind Engineering*, 95–106. <sup>12</sup> 767  
 Bluestein, H. B., and J. H. Golden. 1993. “A review of tornado observa- 768  
 tions.” In Vol. 79 of *Geophysical monograph series*, 319–352. 769  
 Washington, DC: AGU. <https://doi.org/10.1029/GM079p0319>. <sup>13</sup> 770  
 Bluestein, H. B., J. C. Snyder, and J. B. Houser. 2015. “A multiscale 771  
 overview of the El Reno, Oklahoma, Tornadic Supercell of 31 May 772  
 2013.” *Weather Forecasting* 30 (3): 525–552. [https://doi.org/10.1175 773  
 /WAF-D-14-00152.1](https://doi.org/10.1175/WAF-D-14-00152.1). 774  
 Bluestein, H. B., K. J. Thiem, J. C. Snyder, and J. B. Houser. 2018. “The 775  
 multiple-vortex structure of the El Reno, Oklahoma, tornado on 31 776  
 May 2013.” *Mon. Weather Rev.* 146 (8): 2483–2502. [https://doi.org/10 777  
 .1175/MWR-D-18-0073.1](https://doi.org/10.1175/MWR-D-18-0073.1). 778  
 Cao, S., M. Wang, and J. Cao. 2018. “Numerical study of wind 779  
 pressure on low-rise buildings induced by tornado-like flows.” *J. 780  
 Wind Eng. Ind. Aerodyn.* 183 (Dec): 214–222. [https://doi.org/10.1016 781  
 /j.jweia.2018.10.023](https://doi.org/10.1016/j.jweia.2018.10.023). 782  
 Case, J., P. Sarkar, and S. Sritharan. 2014. “Effect of low-rise 783  
 building geometry on tornado-induced loads.” *J. Wind Eng. Ind. 784  
 Aerodyn.* 133 (Oct): 124–134. [https://doi.org/10.1016/j.jweia.2014 785  
 .02.001](https://doi.org/10.1016/j.jweia.2014.02.001). 786  
 Chang, C. C. 1971. “Tornado effects on buildings and structures with lab- 787  
 oratory simulation.” In *Proc., 3rd Int. Conf. on Wind Effects on 788  
 Buildings and Structures*, 231–240. <sup>14</sup> 789  
 Chen, Q., Z. Tang, X. Wu, D. Zuo, and D. James. 2023. “Laboratory 790  
 study of tornado-like loading on a low-rise building model.” *J. Wind 791  
 Eng. Ind. Aerodyn.* 238 (Jul): 105443. [https://doi.org/10.1016/j.jweia 792  
 .2023.105443](https://doi.org/10.1016/j.jweia.2023.105443). 793  
 Church, C., J. T. Snow, G. L. Baker, and E. M. Agee. 1979. 794  
 “Characteristics of tornado-like vortices as a function of swirl ratio: A 795  
 laboratory investigation.” *J. Atmos. Sci.* 36 (9): 1755–1776. [https://doi 796  
 .org/10.1175/1520-0469\(1979\)036<1755:COTLVA>2.0.CO;2](https://doi.org/10.1175/1520-0469(1979)036<1755:COTLVA>2.0.CO;2). 797  
 Dang, J., T. Do, J. van de Lindt, Y. Zhao, L. Orf, and G. Yan. 2023. 798  
 “Tornado fragility of large-box tilt-up buildings based on high-fidelity 799  
 CFD simulations.” In *Proc., ASCE Inspire 2023*, 274–281. [https://doi 800  
 .org/10.1061/9780784485163.033](https://doi.org/10.1061/9780784485163.033). <sup>15</sup> 801  
 Davies-Jones, R., R. J. Trapp, and H. B. Bluestein. 2001. “Tornadoes 802  
 and tornadic storms.” In *Severe convective storms*, 167–221. 803  
 Boston: American Meteorological Society. [https://doi.org/10.1007 804  
 /978-1-935704-06-5\\_5](https://doi.org/10.1007/978-1-935704-06-5_5). 805  
 Davies-Jones, R. P. 1973. “The dependence of core radius on swirl ratio in 806  
 a tornado simulator.” *J. Atmos. Sci.* 30 (7): 1427–1430. [https://doi 807  
 .org/10.1175/1520-0469\(1973\)030<1427:TDOCRO>2.0.CO;2](https://doi.org/10.1175/1520-0469(1973)030<1427:TDOCRO>2.0.CO;2). 808  
 Diamond, C. J., and E. M. Wilkins. 1984. “Translation effects on simu- 809  
 lated tornadoes.” *J. Atmos. Sci.* 41 (17): 2574–2580. [https://doi.org/10 810  
 .1175/1520-0469\(1984\)041<2574:TEOST>2.0.CO;2](https://doi.org/10.1175/1520-0469(1984)041<2574:TEOST>2.0.CO;2). 811  
 Fouts, L., D. L. James, and C. W. Letchford. 2003. “Pressure distribution 812  
 on a cubical model in tornado-like flow.” In *Proc., 10th Int. Wind 813  
 Engineering Conf. Lubbock*. <sup>16</sup> 814  
 Fujita, T. T. 1970. “The Lubbock tornadoes: A study of suction spots.” 815  
*Weatherwise* 23 (4): 161–173. [https://doi.org/10.1080/00431672.1970 816  
 .9932888](https://doi.org/10.1080/00431672.1970.9932888). 817  
 Fujita, T. T. 1981. “Tornadoes and downbursts in the context of gener- 818  
 alized planetary scales.” *J. Atmos. Sci.* 38 (8): 1511–1534. [https://doi 819  
 .org/10.1175/1520-0469\(1981\)038<1511:TADITC>2.0.CO;2](https://doi.org/10.1175/1520-0469(1981)038<1511:TADITC>2.0.CO;2). 820  
 Gairola, A., and G. Bitsuamlak. 2019. “Numerical tornado modeling 821  
 for common interpretation of experimental simulators.” *J. Wind Eng. 822  
 Ind. Aerodyn.* 186 (Mar): 32–48. [https://doi.org/10.1016/j.jweia.2018 823  
 .12.013](https://doi.org/10.1016/j.jweia.2018.12.013). 824  
 Haan, F. L., V. K. Balaramudu, and P. P. Sarkar. 2010. “Tornado-induced 825  
 wind loads on a low-rise building.” *J. Struct. Eng.* 136 (1): 106–116. 826  
[https://doi.org/10.1061/\(ASCE\)ST.1943-541X.0000093](https://doi.org/10.1061/(ASCE)ST.1943-541X.0000093). 827

- 828 Hangan, H., and J. D. Kim. 2008. "Swirl ratio effects on tornado vortices  
829 in relation to the Fujita scale." *Wind Struct.* 11 (4): 291–302. <https://doi.org/10.12989/was.2008.11.4.291>.
- 830 Honerkamp, R., G. G. Yan, and J. van de Lindt. 2022. "Revealing  
831 bluff-body aerodynamics on low-rise buildings under tornadic winds  
832 using numerical laboratory tornado simulator." *J. Struct. Eng.* 148 (3):  
833 04021294. [https://doi.org/10.1061/\(ASCE\)ST.1943-541X.0003283](https://doi.org/10.1061/(ASCE)ST.1943-541X.0003283).
- 834 Ipauley, R. L., and J. T. Snow. 1988. "On the kinematics and dynamics of  
835 the 18 July 1986 Minneapolis tornado." *Mon. Weather Rev.* 116 (12):  
836 2731–2736. [https://doi.org/10.1175/1520-0493\(1988\)116<2731:  
837 OTKADO>2.0.CO;2](https://doi.org/10.1175/1520-0493(1988)116<2731:OTKADO>2.0.CO;2).
- 838 Jischke, M. C., and B. D. Light. 1983. "Laboratory simulation of  
839 tornadic wind loads on a rectangular model structure." *J. Wind  
840 Eng. Ind. Aerodyn.* 13 (1–3): 371–382. [https://doi.org/10.1016/0167  
841 -6105\(83\)90157-5](https://doi.org/10.1016/0167-6105(83)90157-5).
- 842 Karstens, C. D., W. A. Gallus Jr., B. D. Lee, and C. A. Finley.  
843 2013. "Analysis of tornado-induced tree fall using aerial photography  
844 from the Joplin, Missouri, and Tuscaloosa–Birmingham, Alabama,  
845 Tornadoes of 2011." *J. Appl. Meteorol. Climatol.* 52 (5): 1049–1068.  
846 <https://doi.org/10.1175/JAMC-D-12-0206.1>.
- 847 Kuligowski, E. D., F. T. Lombardo, L. T. Phan, M. L. Levitan, and D. P.  
848 Jorgensen. 2014. *Final report, NIST technical investigation of the  
849 May 22, 2011, Tornado in Joplin, Missouri*. Rep. No. NIST  
850 NCSTAR-3. Gaithersburg, MD: NIST.
- 851 Leonard, B. P. 1991. "The ULTIMATE conservative difference  
852 scheme applied to unsteady one-dimensional advection." *Comput.  
853 Methods Appl. Mech. Eng.* 88 (1): 17–74. [https://doi.org/10.1016/0045  
854 -7825\(91\)90232-U](https://doi.org/10.1016/0045-7825(91)90232-U).
- 855 Lewellen, D. C., W. S. Lewellen, and J. Xia. 2000. "The influ-  
856 ence of a local swirl ratio on tornado intensification near the sur-  
857 face." *J. Atmos. Sci.* 57 (4): 527–544. [https://doi.org/10.1175/1520  
858 -0469\(2000\)057<0527:TIOALS>2.0.CO;2](https://doi.org/10.1175/1520-0469(2000)057<0527:TIOALS>2.0.CO;2).
- 859 Li, T., H. Qu, Y. Zhao, R. Honerkamp, G. Yan, A. Chowdhury, and I.  
860 Zisis. 2023. "Wind effects on dome structures and evaluation of CFD  
861 simulations through wind tunnel testing." *Sustainability* 15 (5): 4635.  
862 <https://doi.org/10.3390/su15054635>.
- 863 Li, T., G. Yan, F. Yuan, and G. Chen. 2019. "Dynamic structural respon-  
864 ses of long-span dome structures induced by tornadoes." *J. Wind Eng.  
865 Ind. Aerodyn.* 190 (Jul): 293–308. [https://doi.org/10.1016/j.jweia.2019  
866 .05.010](https://doi.org/10.1016/j.jweia.2019.05.010).
- 867 Liu, Z., and T. Ishihara. 2015. "Numerical study of turbulent flow fields  
868 and the similarity of tornado vortices using large-eddy simulations." *J.  
869 Wind Eng. Ind. Aerodyn.* 145 (Oct): 42–60. [https://doi.org/10.1016/j  
870 .jweia.2015.05.008](https://doi.org/10.1016/j.jweia.2015.05.008).
- 871 Liu, Z., and T. Ishihara. 2016. "Study of the effects of translation and  
872 roughness on tornado-like vortices by large-eddy simulations." *J.  
873 Wind Eng. Ind. Aerodyn.* 151 (Apr): 1–24. [https://doi.org/10.1016/j  
874 .jweia.2016.01.006](https://doi.org/10.1016/j.jweia.2016.01.006).
- 875 Mishra, A. R., D. L. James, and C. W. Letchford. 2008. "Physical simula-  
876 tion of a single-celled tornado-like vortex. Part B: Wind loading on  
877 a cubical model." *J. Wind Eng. Ind. Aerodyn.* 96 (8–9): 1258–1273.  
878 <https://doi.org/10.1016/j.jweia.2008.02.027>.
- 879 Natarajan, D., and H. Hangan. 2012. "Large eddy simulations of trans-  
880 lation and surface roughness effects on tornado-like vortices." *J.  
881 Wind Eng. Ind. Aerodyn.* 104 (May): 577–584. [https://doi.org/10.1016  
882 /j.jweia.2012.05.004](https://doi.org/10.1016/j.jweia.2012.05.004).
- 883 Nicoud, F., and F. Ducros. 1999. "Subgrid-scale stress modelling based  
884 on the square of the velocity gradient tensor." *Flow Turbul. Combust.*  
885 62 (3): 183–200. <https://doi.org/10.1023/A:1009995426001>.
- 886 NSSL (National Severe Storms Laboratory). 1995. *Tornadoes: A prepar-  
887 edness guide including safety information for schools*. US Dept. of  
888 Commerce, NOAA, National Weather Service.
- 889 Razavi, A., and P. P. Sarkar. 2021. "Effects of roof geometry on  
890 tornado-induced structural actions of a low-rise building." *Eng. Struct.*  
891 226 (Jan): 111367. <https://doi.org/10.1016/j.engstruct.2020.111367>.
- 892 Rotunno, R. 2013. "The fluid dynamics of tornadoes." *Annu. Rev. Fluid  
893 Mech.* 45 (1): 59–84. [https://doi.org/10.1146/annurev-fluid-011212  
894 -140639](https://doi.org/10.1146/annurev-fluid-011212-140639).
- 895 Sengupta, A., F. L. Haan, P. P. Sarkar, and V. Balaramudu. 2008.  
896 "Transient loads on buildings in microburst and tornado winds." *J.  
897 Wind Eng. Ind. Aerodyn.* 96 (10–11): 2173–2187. [https://doi.org/10  
898 .1016/j.jweia.2008.02.050](https://doi.org/10.1016/j.jweia.2008.02.050).
- 899 Tang, Z., C. Feng, L. Wu, and D. L. James. 2018. "Characteristics of  
900 tornado-like vortices simulated in a large-scale Ward-type simulator." *Boundary Layer Meteorol.* 166 (2): 327–350. [https://doi.org/10.1007  
901 /s10546-017-0305-7](https://doi.org/10.1007/s10546-017-0305-7).
- 902 Van Doormaal, J. P., and G. D. Raithby. 1984. "Enhancements  
903 of the SIMPLE method for predicting incompressible fluid  
904 flows." *Numer. Heat Transfer* 7 (2): 147–163. [https://doi.org/10.1080  
905 /01495728408961817](https://doi.org/10.1080/01495728408961817).
- 906 Wakimoto, R. M., N. T. Atkins, K. M. Butler, H. B. Bluestein, K.  
907 Thiem, J. C. Snyder, and J. Wurman. 2016. "Aerial damage survey of  
908 the 2013 El Reno tornado combined with mobile radar data." *Mon.  
909 Weather Rev.* 144 (5): 1749–1776. [https://doi.org/10.1175/MWR-D  
910 -15-0367.1](https://doi.org/10.1175/MWR-D-15-0367.1).
- 911 Ward, N. B. 1972. "The exploration of certain features of tornado  
912 dynamics using a laboratory model." *J. Atmos. Sci.* 29 (6):  
913 1194–1204. [https://doi.org/10.1175/1520-0469\(1972\)029<1194:TEO  
914 CFO>2.0.CO;2](https://doi.org/10.1175/1520-0469(1972)029<1194:TEO-CFO>2.0.CO;2).
- 915 Wurman, J. 1999. "Preliminary results from the Radar Observations of  
916 Tornadoes and Thunderstorms Experiment (ROTATE-98/99)." In  
917 *Proc., 29th Int. Conf. on Radar Meteorology*, 613–616.
- 918 Wurman, J. 2002. "The multiple-vortex structure of a tornado." *J.  
919 Weather Forecasting* 17 (3): 473–505. [https://doi.org/10.1175/1520  
920 -0434\(2002\)017<0473:TMVSOA>2.0.CO;2](https://doi.org/10.1175/1520-0434(2002)017<0473:TMVSOA>2.0.CO;2).
- 921 Wurman, J., K. Kosiba, P. Robinson, and T. Marshall. 2014. "The role  
922 of multiple-vortex tornado structure in causing storm researcher fatal-  
923 ities." *Bull. Am. Meteorol. Soc.* 95 (1): 31–45. [https://doi.org/10.1175  
924 /BAMS-D-13-00221.1](https://doi.org/10.1175/BAMS-D-13-00221.1).
- 925 Yuan, F., G. Yan, R. Honerkamp, K. M. Isaac, M. Zhao, and X. Mao. 2019.  
926 "Numerical simulation of laboratory tornado simulator that can produce  
927 translating tornado-like wind flow." *J. Wind Eng. Ind. Aerodyn.* 190 (Jul):  
928 200–217. <https://doi.org/10.1016/j.jweia.2019.05.001>.
- 929 Zhang, D., Z. Liu, X. Jiang, W. Jiang, H. Gao, C. Li, Y. Xiao, and G.  
930 Hu. 2023. "Numerical study of flow characteristics of tornado-like  
931 vortices considering both swirl ratio and aspect ratio." *J. Wind Eng.  
932 Ind. Aerodyn.* 240 (Sep): 105468. [https://doi.org/10.1016/j.jweia.2023  
933 .105468](https://doi.org/10.1016/j.jweia.2023.105468).
- 934 Zhang, W., and P. P. Sarkar. 2012. "Near-ground tornado-like vortex  
935 structure resolved by particle image velocimetry." *Exp. Fluids* 52 (2):  
936 479–493. <https://doi.org/10.1007/s00348-011-1229-5>.
- 937 Zhao, Y., G. Yan, and R. Feng. 2021. "Wind flow characteristics of  
938 multivortex tornadoes." *Nat. Hazards Rev.* 22 (3): 04021015. [https://doi.org/10.1061/\(ASCE\)NH.1527-6996.0000462](https://doi.org/10.1061/(ASCE)NH.1527-6996.0000462).
- 939 Zhao, Y., G. Yan, R. Feng, H. Kang, and Z. Duan. 2023. "Influence of  
940 swirl ratio and radial Reynolds number on wind characteristics of  
941 multi-vortex tornadoes." *Adv. Struct. Eng.* 26 (1): 89–107. [https://doi  
942 .org/10.1177/13694332221119867](https://doi.org/10.1177/13694332221119867).